

Dark Matter Halos within Clusters

Sebastiano Ghigna, Ben Moore, Fabio Governato

Department of Physics, University of Durham, Durham DH1 3LE, UK.

George Lake, Thomas Quinn, and Joachim Stadel

Department of Astronomy, University of Washington, Seattle, WA 98195, USA.

Email: S.S.Ghigna@durham.ac.uk

December 1997

ABSTRACT

We examine the properties of dark matter halos within a rich galaxy cluster using a high resolution simulation that captures the cosmological context of a cold dark matter universe. The mass and force resolution permit the resolution of 150 halos with circular velocities larger than 80 km s^{-1} within the cluster’s virial radius of 2 Mpc. This enables an unprecedented study of the statistical properties of a large sample of dark matter halos evolving in a dense environment. The cumulative fraction of mass attached to these halos varies from 0% at 200 kpc, to 13% at the virial radius. Even at this resolution the overmerging problem persists; halos that pass within 200 kpc of the cluster center are tidally disrupted. Additional substructure is lost at earlier epochs within the massive progenitor halos. The median ratio of apocentric to pericentric radii is 6:1; the orbital distribution is close to isotropic, circular orbits are rare, radial orbits are common. The orbits of halos are unbiased with respect to both position within the cluster and with the orbits of the smooth dark matter background and no velocity bias is detected. The tidal radii of surviving halos are generally well-fit using the simple analytic prediction applied to their orbital pericenters. Halos within clusters have higher concentrations than those in the field. Within the cluster, halo density profiles can be modified by tidal forces and individual encounters with other halos that cause significant mass loss - “galaxy harassment”. Mergers between halos do not occur inside the clusters virial radius.

Key words: cosmology: theory – dark matter – large-scale structure of the Universe – galaxies: clusters – galaxies: halos – methods: numerical

1 INTRODUCTION

Rich clusters of galaxies are large cosmological laboratories that may provide unbiased mixtures of the matter content of the Universe (White *et al* 1993, Evrard 1997). Clusters are prominent structures in the Universe; their evolution can be followed with samples out to $z \sim 1$ (Rosati *et al* 1998). They are the most massive virialised objects in the Universe and are the most recent objects to form in hierarchical formation models. Their masses can be determined by several independent methods (e.g. Carlberg *et al* 1997, Cen 1997, Wu & Fang 1997, Smail *et al* 1997).

The evolution of the mass function of clusters is sensitive to key cosmological parameters (e.g. Bahcall, Fan & Cen 1997, Bartelmann *et al* 1997, Borgani *et al* 1997, Carlberg *et al* 1996, Eke, Cole & Frenk 1997, Wilson, Cole & Frenk 1996). This evolution can be calculated by using ei-

ther analytic methods (Press & Schechter 1974) or cosmological N-body simulations (Eke *et al* 1997). The weakness of analytic methods is their inability to follow halos that accrete into larger systems. In the past, numerical simulations have shared this problem. To sample a large volume, the poor resolution within virialised systems leads to soft, diffuse halos that are rapidly dissolved by tidal forces. This is the classic over-merging problem (White *et al* 1987) that has led to problems when comparing the mass distribution within dark matter simulations to the observed properties of galaxies (Summers *et al* 1995).

We were determined to perform simulations that resolved the distribution and evolution of galaxy halos within clusters. There are many questions that we will address with these simulations: What is the orbital distribution of the galaxies within clusters and are they biased in any way? What is the extent of galactic dark halos within clusters

and how much of the cluster’s mass distribution is attached to galaxies? How do these properties evolve with time and within different cosmological models? Are the density profiles of isolated “field” halos similar to the halos that form within the environment of a rich cluster? How does the cluster environment modify the internal structure of halos? The frequency of mergers between halos within the cluster environment and the heating rate from halo–halo encounters are questions of importance for studies of the morphological evolution of clusters. These are amongst the many questions that have remained unanswered due to the over-merging problem.

Some have suggested that the only way to avoid merging is to follow the evolution of the baryons—even if they are only $\sim 5\%$ of the mass (Evrard *et al* 1994). This assertion seems counter-intuitive; it’s now clear that mass and force resolution can overcome the overmerging problem in dark matter simulations (cf. Moore, Katz & Lake 1996, Klypin, Gottlöber & Kravtsov 1997, Brainerd, Goldberg & Villumsen 1997, Moore *et al* 1997). With fast parallel computers and highly tuned algorithms, our simulations have hundreds of surviving halos within the virial radius of a rich cluster (Moore *et al* 1997). Increased mass and force resolution lead to higher central densities in galactic halos, enabling greater survival within a cluster. For the first time we can compare the mass distribution with the galaxy distribution in a rich cluster.

The plan of this paper is as follows: In §2, we describe the N-body simulation, techniques and parameters. In §3 we describe two algorithms to identify “halos within halos”. After creating a catalogue of halos, §4 turns to results on their global properties; sizes, masses, radial distribution, orbital properties and merger histories. §5 discusses the internal properties of halos: their density profiles, correlations between structure parameters and global parameters and the evolution of these quantities with time. We conclude in §6.

2 THE N-BODY SIMULATION

One of the goals of performing cosmological numerical simulations is to compare the distribution and bulk properties of dark matter with the distribution and properties of the observable galaxies. A direct comparison has never been possible, since structure in high density regions has been quickly erased as a consequence of numerical resolution – the overmerging problem. “Galaxies” are typically selected from the mass distribution in a cosmological simulation using a biased sample of dark matter particles. Previous studies of cluster substructure have been limited to using “galaxy tracers” (Carlberg 1991, Summers *et al* 1995), such as following the most bound particle of a halo before it becomes disrupted by the tidal field of the system. These heuristics enable the use of low resolution simulations, but their validity is anyone’s guess at this point (Summers *et al* 1995).

There are now several codes that are able to simulate a gaseous component. Although these codes are invaluable for many astrophysical problems; the original motivation behind these techniques was the hope of resolving galaxies in a cosmological context, thus solving the overmerging problem. They hoped to form galaxies and preserve them by increasing the central densities owing to gas dynamics. In turn, the

halos would be more robust to disruption. Indeed, SPH simulations of individual clusters, do give rise to a set of galaxy tracers that resemble a “real” cluster. However, the mass resolution in the dark matter component is not sufficient to resolve the dark halos of the galaxy tracers, typically one is left with a cold gas blob orbiting within the smooth cluster background (Frenk *et al* 1996). There are a variety of pathologies that arise if one uses too few particles to simulate a large dynamic range in scales. Our simulations are designed to resolve scales of 5 kpc using dark matter. This would be a minimal resolution to simulate galaxy formation with gas dynamics. One needs a fiducial dark matter simulation at high resolution to see differences owing to gas dynamics. One must insure that these differences are sensible as an external check. With the gas representing $\lesssim 10\%$ of the mass, gross changes in numbers and orbits of galaxies would be surprising.

Our aim is to achieve very high spatial and mass resolution within a rich virialised cluster drawn from a “fair volume” of 100 Mpc^3 in a standard CDM Universe. In such a volume, there are several rich clusters, and none dominate the environment in an undesirable way. Any simulation method limits the number of particles that can be invested in a single simulation. Previous simulations of clusters suffered limitations due to the small volume used, forcing the run to stop at $z \sim 1$, (Evrard, Summers & Davis 1994), or the use of vacuum boundary conditions outside the cluster (Carlberg 1991).

With current technology, we can perform a single large simulation of $\sim 10^8$ particles or try to tackle a number of different problems using simulations with $\sim 10^7$ particles. If we simulate our “fair volume” at uniform resolution, there will be $\sim 10^4$ particles within the virial radius of a cluster, a resolution that is insufficient to resolve substructure. Previous attempts to resolve the inner structures of cluster halos using $\sim 10^5$ particles failed to resolve more than a handful of satellite halos (Carlberg 1991, Carlberg & Dubinski 1991, Tormen 1997, Tormen *et al*). To achieve higher resolution within an individual cluster we initially perform a simulation of a large volume of a CDM universe as described above, normalised such that $\sigma_8 = 0.7$ and the shape parameter $\Gamma = 0.5$ ($H=50 \text{ km s}^{-1} \text{ Mpc}^{-1}$ is adopted throughout).

We used a nesting scheme that we call “volume renormalization” to achieve higher resolution within a region of greater interest. This technique has been used to probe quasar formation at high redshift (Katz *et al* 1994) and to follow the density profiles of halos in a cosmological context (Navarro *et al* 1996). We generate initial conditions (ICs) for the volume at two resolutions, one that places $\sim 10^7$ particles within the entire volume and one such that there would be $\lesssim 10^6$ particles in the targeted cluster. We run the lower resolution model and select a virialised cluster at $z = 0$. The particles within about twice the virial radius of the cluster in the final state are traced back to their locations in the ICs. Within this region, we use the higher resolution ICs. Beyond this high resolution region the mass resolution is decreased in a series of shells by combining particles in the high resolution ICs at their center of masses. In this way, the external tidal field is modelled correctly. The starting redshift in the high resolution run is increased to $z=69$ such that the perturbations in the smoothed density field of the high reso-

lution region obey the constraint $\delta\rho/\rho \lesssim 0.1$. We then re-run the simulation to the present epoch.

We use a new high performance parallel treecode “PKDGRAV” to evolve the particle distribution. PKDGRAV (Stadel *et al.*, in preparation) has accurate periodic boundaries and an open ended variable timestep criteria based upon the local acceleration (Quinn *et al.* 1997). The code uses a spline softening length such that the force is completely Newtonian at twice our quoted softening lengths. In terms of where the force is 50% of the Newtonian force, the equivalent Plummer softening length would be 0.67 times the spline softening length. In the high resolution region, our particle mass is $8.6 \times 10^8 M_\odot$. We perform two runs with 10 kpc (RUN1) and 5 kpc (RUN2) softening lengths. The final virial radius of the cluster is ~ 2 Mpc and the mass is $4.6 \times 10^{14} M_\odot$ so that we have approximately 600,000 particles within a sphere of overdensity 200. (Note that the cluster that is analysed here is the “Virgo” cluster from Moore *et al.* 1997.)

3 CLUSTER SUBSTRUCTURE AND HALO IDENTIFICATION

3.1 The density distribution in the cluster

In past work, halos in dissipationless N -body simulations have usually spontaneously dissolved when entering clusters. Two physical effects conspire with the finite numerical resolution to erase dark matter halos in clusters (Moore, Katz & Lake 1996). Halos are heated by cluster tides and halo-halo encounters, thus losing mass as they move into the potential well. When the tidal radius approaches ~ 3 times their “core radii” (owing to either a density plateau or gravitational softening), they dissolve. Hence, it takes very high resolution to retain dark matter substructures at a distance 100-200 kpc from the cluster’s center. Our numerical parameters were chosen so that halos would survive at these scales. The wealth of halos retained in our simulated cluster is visible in Figure 1

The upper panel is a map of the density distribution in a box of size R_{200} (see §3.2 for a precise definition), centered on the cluster and projected onto a plane. Each particle is colour coded according to the logarithm of the local density (defined using an SPH smoothing kernel over 64 particles in a code called *SMOOTH* [Stadel & Quinn 1997, [http ref: http://www-hpcc.astro.washington.edu/tools](http://www-hpcc.astro.washington.edu/tools)]). Only regions with density contrast $\delta > 30$ are shown. The cluster boundaries, set at R_{200} , correspond to the contours of the central blue region. Much of the mass inside R_{200} lies in the dark matter halos that we will analyze here. Their projected distribution is shown as a ‘circle plot’ in the lower panel of Figure 1. The radius of each circle is the halo ‘tidal radius’ (Sec. 3.3) in units of R_{200} . Note that halos of similar central densities (similar colour in the density map) may have largely different radii depending on their distances from the cluster’s center. It is remarkable that substructure halos cover such a large fraction of the projected cluster’s area.

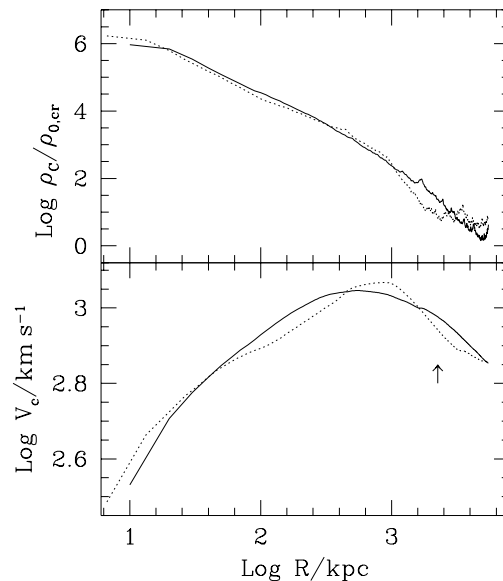


Figure 2. The density (upper panel) and circular velocity (lower panel) profiles for the cluster. The solid curves are at the final epoch and the dotted curves show the cluster at a redshift $z = 0.5$. The density is measured in units of the present critical density $\rho_{0,cr}$; R is the physical distance to the cluster center, and was set at the location of the most bound particle. The arrow marks the value of the cluster virial radius R_{200} at $z = 0$.

3.2 Cluster properties and evolution

We define the cluster center as the position of its most bound particle. This particle is within a softening length of the center of the most massive halo found by SKID. The density profile of the RUN1 cluster calculated in spherical shells is shown in the upper panel of Figure 2 (the solid line is for $z = 0$ and dotted line for $z = 0.5$). The cluster forms at $z \sim 0.8$ from the mergers of many halos along a filamentary structure and, at $z = 0.5$, it has not yet virialised since it still has quite a lumpy structure but the global density profile is roughly similar to that measured 5 Gyrs later at $z=0$. (We shall compare properties of the substructure identified at both epochs.)

The lower panel of this figure shows the circular velocity profile $V_c(R) \equiv (GM(R)/R)^{1/2}$, where $M(R)$ is the mass within R . The virial radius of the cluster is defined as the distance R_{200} for which the average density enclosed, $\bar{\rho}_C(R_{200})$, is 200 times the cosmic density, ρ_{cr} ; we obtain $R_{200} = 1.95$ Mpc at $z = 0$ and 1.2 Mpc at $z = 0.5$. The cluster is not spherical and has axial ratios that are roughly 2:1:1. (In the following we will always use units of kpc and km s^{-1} for lengths and velocities, unless we explicitly state otherwise.)

Figure 3 shows the growth of the cluster’s mass with redshift. Defining the formation redshift of the cluster as that where it has accreted half of its final mass, $z_{form} \sim 0.8$ for our cluster. This is slightly earlier than expected for an average cluster of this mass from the Press-Schechter theory (1974; Lacey & Cole 1993), where $z_{form} \sim 0.5$ (as calculated from a routine kindly supplied by Paolo Tozzi).

COLOUR PLOT

figure1.jpg

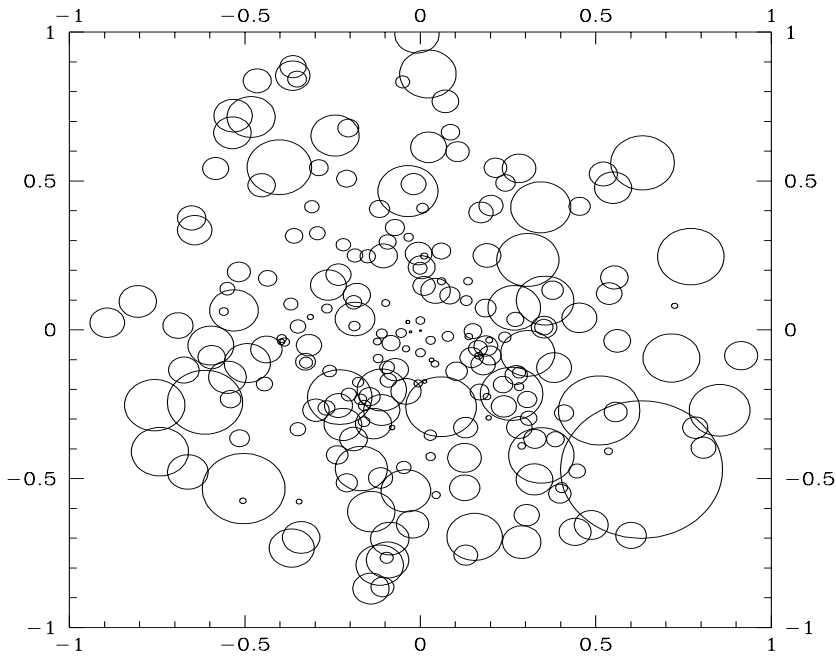


Figure 1. Density map (colour plot) and circle plot of the halo radii within the cluster's virial radius (taken here as the length unit) at $z = 0$.

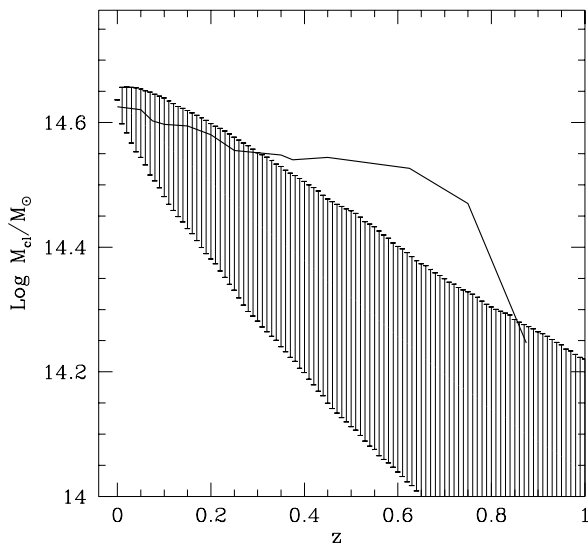


Figure 3. Growth of the cluster’s mass M_{cl} with redshift z . M_{cl} is the mass encompassed by the cluster’s ‘virial’ radius at each z . The errorbars delimit the $1-\sigma$ confidence interval for the growth rate predicted using the Press-Schechter theory.

This is not an unwelcome feature, since the cluster is in true virial equilibrium at $z = 0$.

3.3 Halo identification

Identifying DM halos in the high-density environment of the cluster is a critical step (cfr. Klypin, Gottlöber & Kravtsov 1997). The halos jump out visually, so while it is relatively straightforward to identify the halo centers, we must select only the bound particles to characterize the halo. We want to screen the cluster background that’s streaming through, but the substructure itself will be tidally distorted and may have tidal tails of material that are loosely attached to the halo. Our group finding algorithm uses local density maxima to find group centers and then iteratively checks for self-boundedness to define group membership. Each *group* of particles found belongs to an individual *halo*. The algorithm is an improved version of DENMAX (ref), named SKID and is fully described by Stadel *et al* (1996, see [http ref: http://www-hpcc.astro.washington.edu/tools](http://www-hpcc.astro.washington.edu/tools)). For each simulation we adopt a linking length of $1.5l_{soft}$ and a minimum number of member particles of 16, corresponding to a mass of $\simeq 1.35 \cdot 10^{10} M_{\odot}$. In general, we shall use halos with more than 16 particles when they are employed as tracers, but we shall adopt a minimum number of 32 particles when their individual properties are relevant.

The high resolution region that we analyze is roughly the turn-around radius of the cluster or about twice the virial radius, $R_{ta} \simeq 2R_{200} \simeq 5$ Mpc. Within this radius, there are 495 and 522 halos for RUN1 and RUN2, and 208 and 227 halos respectively within R_{200} . Changing l_{soft} by a factor of two does not make much difference on a global scale, but if we restrict ourselves to the inner parts of the cluster the difference between the numbers of halos changes

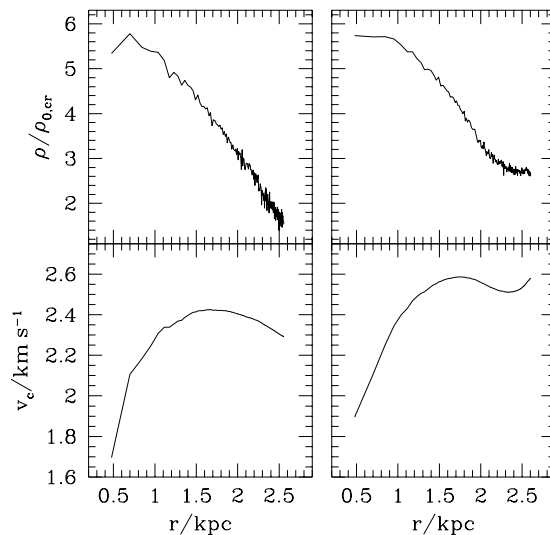


Figure 4. Density profiles and circular velocity profiles are plotted for two large dark matter halos extracted from the simulation. The left panel is a “peripheral” halo that lies beyond the main cluster’s virial radius at $R = 4.2$ Mpc. The halo in the right panel lies within the cluster at $r = 1.2$ Mpc. The radius r measures the distance from the center of each halo. In the latter case, the radius at which the high density background of cluster particles dominates the halo particle distribution is apparent as a flattening of $\rho(r)$ and the linear rise of $v_c(r)$ in the outer regions. We denote the peak value of the circular velocity as v_{peak} and the radius at which it occurs as r_{peak} .

significantly: Inside $R < R_{200}/2$, RUN2 has 91 halos compared to the 59 found in RUN1 and RUN2 has twice as many within $R < R_{200}/4$ (30 instead of 16). The innermost halos in RUN1 and RUN2 are at ~ 200 kpc and ~ 100 kpc respectively. These differences reflect the softening length’s effect on the halos’ central densities that determine their survival against tidal disruption (Moore *et al* 1997; see also the discussion related to Figure 5 below). Quality control of our halo finding algorithm was insured by visually inspecting the density distribution inside R_{200} to verify that we neither missed nor created structures.

We use the output of SKID to determine the halo structural parameters. In particular, it estimates the extent of a halo using the distance to the least bound particle. However, the full 6-dimensional phase space information is never available in the real Universe, therefore we shall compare results from SKID using an “observable” quantity for each halo. For example, the (projected) mass distributions can be determined using either weak lensing, the rotation curves of spirals or the velocity dispersion profiles of ellipticals. Motivated by gravitational lensing, one possibility is to define a halo’s radius using its density profile $\rho(r)$, where r is the distance from a halo’s center, and measuring the radius ($\equiv r_{\rho}$) at which the local density of the cluster background dominates and $\rho(r)$ flattens (cfr. fig. 4). Rotation curves or velocity dispersion profiles of isolated objects will eventually decline with radius, but if a halo is embedded within a deeper

potential, at some radius its profile will turn around and increase as the velocity dispersion of the cluster background starts dominating. (Figure 4 shows that the position of these inflexion points are essentially equal.) We therefore combine these two definitions and use the inflexion point ($\equiv r_{vc}$) of the effective circular velocity $v_c = (GM(r)/r)^{1/2}$ as an alternative independent estimate of the extent of a halo (cfr. fig. 4).

The circular velocity is less noisy than the density or velocity dispersion and thereby more suitable for an automated procedure. Moreover, the inflexion point of $v_c(r)$ can be easily detected by searching for a minimum, without any knowledge of the background density (as it would be necessary, if we were to implement an overdensity criterium). The radius r_{vc} can either overestimate r_ρ , for steeply declining velocity profiles, or underestimate it, for profiles close to isothermal. If the halos are described by the NFW model (Navarro, Frenk & White 1996; see also Section 5), the former condition applies to halos with $v_c \sim 50 \text{ km s}^{-1}$ and the latter to halos with $v_c \gtrsim 200 \text{ km s}^{-1}$ for background densities ~ 300 times the cosmic average (as we will see however, the profiles of tidally ‘stripped’ halos decline with r more steeply than an NFW profile). In our case, for small halos, the difference can be at most $\sim 10\%$; as for large halos, r_{vc} differs from r_ρ by $\lesssim 20\%$ in about 1/3 of the halos in our sample with $v_c \gtrsim 120 \text{ km s}^{-1}$. These differences do not significantly affect our results. With this definition, there is a contribution to the mass encompassed by a halo from the smooth background of order 20%, which we subtract from the quoted halo masses.

For each SKID halo, we calculate $\rho(r)$ and $v_c(r)$ using equally spaced bins of 2 kpc, such that the number of particles in each bin is nearly equal. The departure of $\rho(r)$ from isothermality is betrayed by a peak of $v_c(r)$, v_{pk} occurring at r_{pk} . The catalog values of r_{pk} and v_{pk} are estimated by fitting a cubic spline to $v_c(r)$. The left panels of Figure 4 show a sample $\rho(r)/\rho_{0,cr}$ and $v_c(r)$ curves for a large peripheral halo at a distance of $R = 4.2 \text{ Mpc}$ from the center of RUN1 (hereafter *cluster halos* are those within R_{200} , and *peripheral halos* those between R_{200} and R_{ta}).

Halos beyond the cluster boundary can be easily characterized by their ‘virial’ radii and masses $M_{200} \equiv M(r_{200})$. For isothermal spheres the circular velocity at r_{200} is $v_{200} = (r_{200}/\text{kpc})h \text{ km s}^{-1}$ to within a few percent. For the halo mentioned above, $r_{200} \simeq 400 \text{ kpc}$ ($M_{200} = 3.4 \cdot 10^{12} M_\odot$). The right panels of Figure 4 show $\rho(r)/\rho_{0,cr}$ and $v_c(r)$ for a tidally limited massive cluster halo at $R = 1.2 \text{ Mpc}$, where $\rho_{bkg} \simeq 300\rho_{0,cr}$. The halo radius r_{halo} is either the virial radius, r_{200} or the *tidal radius* r_{tid} , as appropriate. Similarly, the halo mass is defined as $M_{halo} \equiv M(r_{halo}) = v_c(r_{halo})^2 r_{halo}/G$.

Force softening and the finite mass resolution introduce halo cores that are visible in Figure 4 as a flattening of $\rho(r)$ at $r \lesssim 10 \text{ kpc}$. We define a *core radius* r_{core} for each halo as the radius where v_c has risen to 70% of v_{peak} .

Once the halo positions and structural parameters are known, we can start to address the questions raised in the Introduction. We begin by examining the global properties of the halo distribution, with a preliminary discussion of numerical resolution effects.

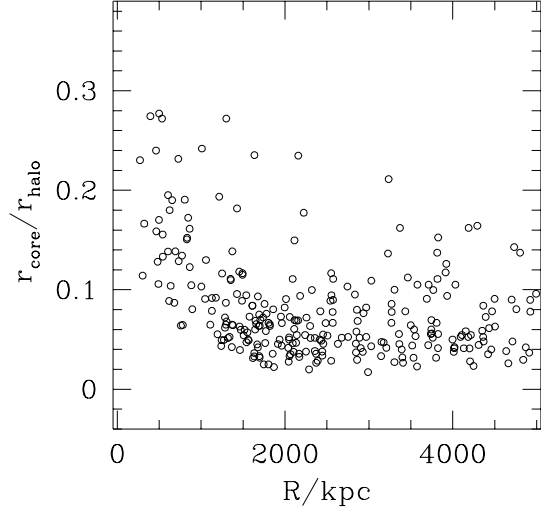


Figure 5. For every halo within $R = 5 \text{ Mpc}$ we plot the ratio of halo core radii and outer radii vs. clustercentric position. Halos contain at least 32 particles.

4 PROPERTIES OF THE HALO DISTRIBUTION

4.1 Numerical resolution effects

Halo in clusters are ‘harassed’ by encounters with other halos combined with strong global tides. This adds internal energy and leads to mass loss. Using a static cluster potential, Moore, Katz & Lake (1996) found that halos rapidly disrupt when $r_{tidal} < 3-4r_{core}$. Our fully self-consistent simulations verify this. Figure 5 shows the ratios r_{core}/r_{halo} vs R for our halo set using RUN1. This ratio increases towards the cluster center and no halos exist with $r_{core}/r_{halo} \gtrsim 0.3$. (Similar results hold for RUN2.) Clearly, the softening will set a floor to the core radius, but in general we find that $r_{core} \sim l_{soft}$, and correspondingly, that halos smaller than $\sim 3l_{soft}$ have all dissolved. The lower boundary for r_{halo} in RUN1 and RUN2 is indeed ~ 30 and $\sim 15 \text{ kpc}$ respectively.

Numerical limitations can also be seen in Figure 6, a plot of v_{peak} versus R for RUN1. There is no bias apparent in this plot, halos of all circular velocity exist over a wide range in R . We show two curves that exclude regions of space owing to our numerical resolution: (i) defining a minimum particle number to identify halos sets a lower mass limit, $M_{lim} = 1.35 \cdot 10^{10} M_\odot$, (ii) r_{tidal} is correlated with R and halos dissolve when $r_{tidal} \gtrsim 3r_{core} \simeq 3l_{soft}$. Approximating the halos as isothermal spheres that are tidally stripped like layers off an onion, the mass and circular velocity are related as: $M_{halo} \equiv M_{200} = Gv_c^2 r_{200}$ for unstripped peripheral halos and $M_{halo} \simeq Gv_c^2 r_{tid}$ for ‘stripped’ cluster halos. The tidal radius obtained from v_c through $r_{tid} \simeq Rv_c/V_c$ ($V_c \simeq 1000 \text{ km s}^{-1}$ is the circular velocity for the cluster) in the approximation that a halo at R is tidally truncated ‘locally’, i.e. according to the value of $\bar{\rho}_C$ at R (this is a limiting case as their pericentric radius can only be smaller). Applying condition (i) leads to the dotted line in Figure 6; crite-

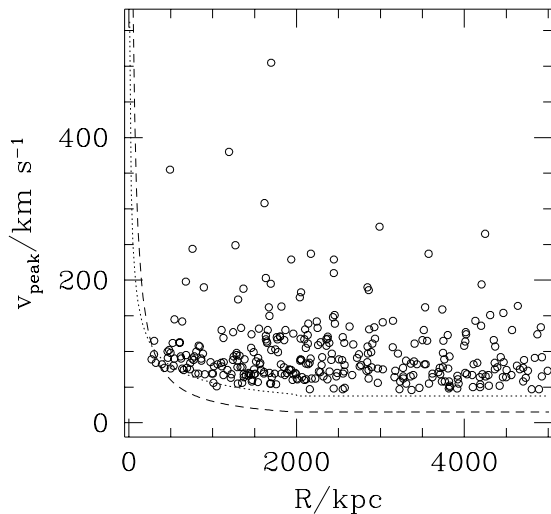


Figure 6. The peak circular velocities of halos, v_{peak} , is plotted against their clustercentric position R at $z = 0$. The lines give the expected limiting R at which halos of given v_{peak} can be resolved because of the finite spatial resolution (dashed curve) and mass resolution (dotted line).

tion (*ii*) leads to the dashed line (we set $v_c = \text{const} = v_{peak}$). If tides due to the cluster potential are the only cause of halo disruption, our sample should be complete for halos with $v_{peak} \gtrsim 80 \text{ km s}^{-1}$ and pericenters that have always been greater than $R_{lim} \sim 250 \text{ kpc}$.

4.2 Spatial distribution of halos

The number density of halos, n_{halos} , is plotted against R in Figure 7, for the two runs. The dashed line refers to the particle density, n_{part} , normalised to the halo density in the interval $[R_{200}, R_{ta}]$.

Beyond the cluster’s virial radius the curves for halos and particles have similar slopes. Within the cluster’s virial radius we see that the halo distribution is “antibias”, *i.e.* less concentrated, with respect to the mass distribution. The halo number density profile is consistent, for $R > 1 \text{ Mpc}$, with the average galaxy number density profile derived by Carlberg *et al* (1997) for the clusters of the CNOC survey. However, the average cluster mass profile that they derive from the same data is much shallower than that of the relatively small cluster analyzed here.

If we regard the scaled particle distribution as the “asymptotic” halo distribution in the case of no bias and infinite resolution (and sufficiently small physical cores), then we can estimate the numbers of missing halos by integrating the difference over R . For RUN2 we find that ~ 240 halos are “missing”, about 50% of the halos with $v_{peak} > 80 \text{ km s}^{-1}$. The systematic difference between RUN1 and RUN2 makes tidal disruption of “softened” halos the most likely cause of this bias. However, the destruction of halos may not be due to numerical resolution alone. For example, binary mergers between halos of similar mass will lead to a single halo

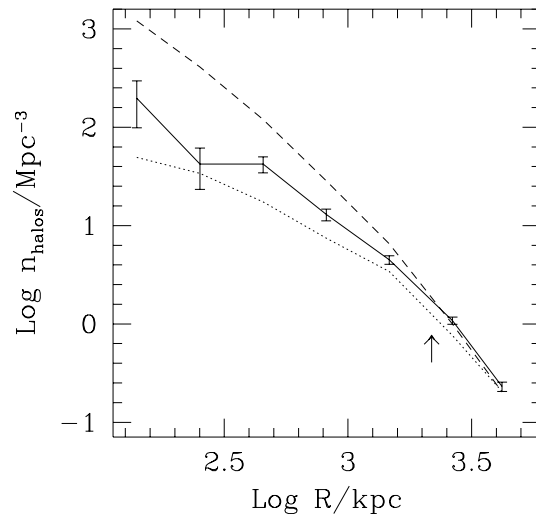


Figure 7. The number density of halos with $v_{peak} \geq 80 \text{ km s}^{-1}$ as a function of R , for RUN1 (dotted line) and RUN2 (solid line); the former has a spline softening length of 10 kpc, twice that of the latter. The dashed line is the particle density scaled in such a way that, in the distance interval $[R_{200}, R_{ta}]$, the scaled number of particles equals the number of halos. The errorbars are $1\text{-}\sigma$ Poissonian errors from the counts in each bin; the arrow marks the value of R_{200} .

with no memory of its history. This halo anti-bias may be overcome with higher resolution simulations that accurately resolve the structure of the smallest halos.

4.3 Distribution of halo radii

The extent of dark matter halos attached to galaxies in clusters has become directly observable via observations of gravitational lensing (Geiger & Bartelmann 1997, Natarajan *et al* 1997). Here we can make some predictions for future surveys that will constrain the extent of halos as a function of position from the cluster center.

The projected distribution of the halos within the cluster’s boundaries was shown in the lower panel of Fig. 1. There is a clear decrease of halo sizes near the cluster’s center even in this projected plot (there is little difference if we include halos up to twice R_{200}).

Figure 8 shows the average value of r_{halo}/R_{200} as a function of clustercentric position, R/R_{200} , at redshifts $z=0$ and $z=0.5$. We use R_{200} at each z as the length unit to highlight the self-similarity in the evolution of the cluster substructure. Halo radii clearly decrease as we move towards the cluster center, but the trend is hard to detect at $z = 0.5$ because the cluster has accreted only relatively few halos (of $v_{peak} > 80 \text{ km s}^{-1}$), has a quite anisotropic mass distribution and tides have been efficient only in its very center. The mean size of halos beyond R_{200} is $\gtrsim 8\%$ of R_{200} and drops approximately linearly to zero as we move from the virial radius to the cluster center. (In Fig. 8, halo radii are those measured from the circular velocity profiles; the results using

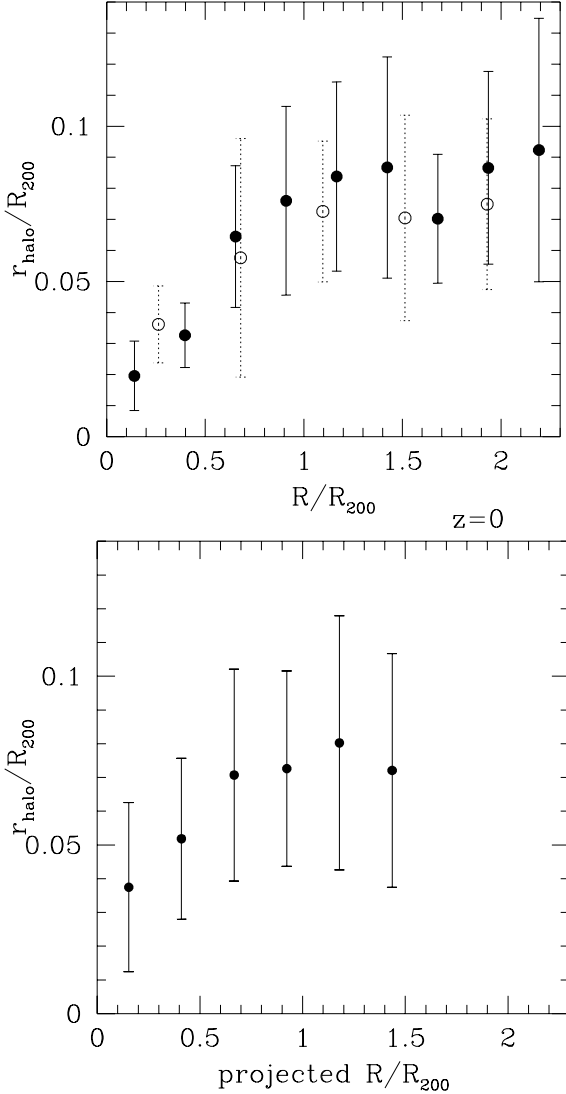


Figure 8. In the upper panel, the average value of halo radii plotted against cluster-centric position at redshift $z = 0$ (solid symbols) and $z = 0.5$ (dotted), for halos with $v_{\text{peak}} \geq 80 \text{ km s}^{-1}$. The lower panel shows the distribution against projected distance at $z = 0$. At each z , the unit is the cluster’s virial radius at that epoch. The errorbars give the dispersion about the average. Note that the most massive cluster halo at $z = 0$ has been excluded from the average; it has a radius of 470 kpc and is located at $R = 0.9R_{200}$.

SKID radii are very similar.) As shown in the lower panel of this Figure, projection effects weaken but do not erase the trend of halo radii with R (here we have included halos up to $1.5R_{200}$, but it makes little difference changing the limiting R between once and twice R_{200}). Natarajan et al. (1997) do not detect a dependence on R , but presently, the observational uncertainties are large and the radial range of the data is limited.

Halos of different v_{peak} obviously have intrinsically different sizes. We can interpret Figure 8 and account for this intrinsic scatter using our “locally stripped isothermal onion approximation” (with $v_c \equiv v_{\text{peak}}$; see Section 4.1)

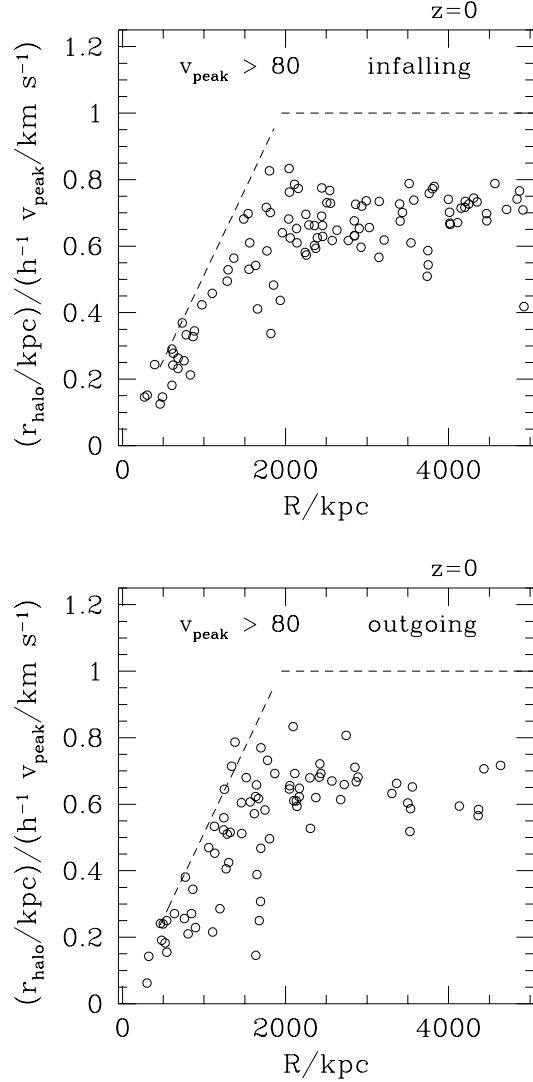


Figure 9. The figure highlights the effects of tidal stripping on halo sizes at varying distance from the cluster’s center (halos with $v_{\text{peak}} > 80 \text{ km s}^{-1}$). For our halo sample, the ratio $r_{\text{halo}}h/v_{\text{peak}}$, with $h = h_0(1+z)^{1.5}$ and units of kpc and km s^{-1} , is approximately 70% of the value expected for a purely isothermal mass distribution. The dashed line gives the expected behaviour for isothermal halos being instantaneously stripped whilst falling into the deeper potential of the cluster. The upper and lower panels are for inwards and outwards moving halos respectively. See the text for further details.

and considering the ratios $\eta \equiv r_{\text{halo}}/(h^{-1}v_{\text{peak}})$. When halos form in isolation, $r_{\text{halo}} \equiv r_{200} \approx h^{-1}v_c$ and $\eta \simeq \text{const} \simeq 1 \cdot \text{kpc}/\text{km s}^{-1}$. Within the cluster, $r_{\text{halo}} \equiv r_{\text{tid}} \simeq Rv_c/V_c \simeq (h^{-1}v_c)R/R_{200}$ and $\eta(R) \simeq R/R_{200}$. If halos have gone past pericenter r_{peri} and their radii r_{tid} are determined by $\bar{\rho}_C(r_{\text{peri}})$, then η will be smaller by a factor of r_{peri}/R (cfr. Fig. 17 in Sec. 4.6).

In a fully virialized system there is no difference between the motions away and towards the system’s center. However, in a $\Omega = 1$ cosmology, clusters never stop accreting material and we might expect some different morpholo-

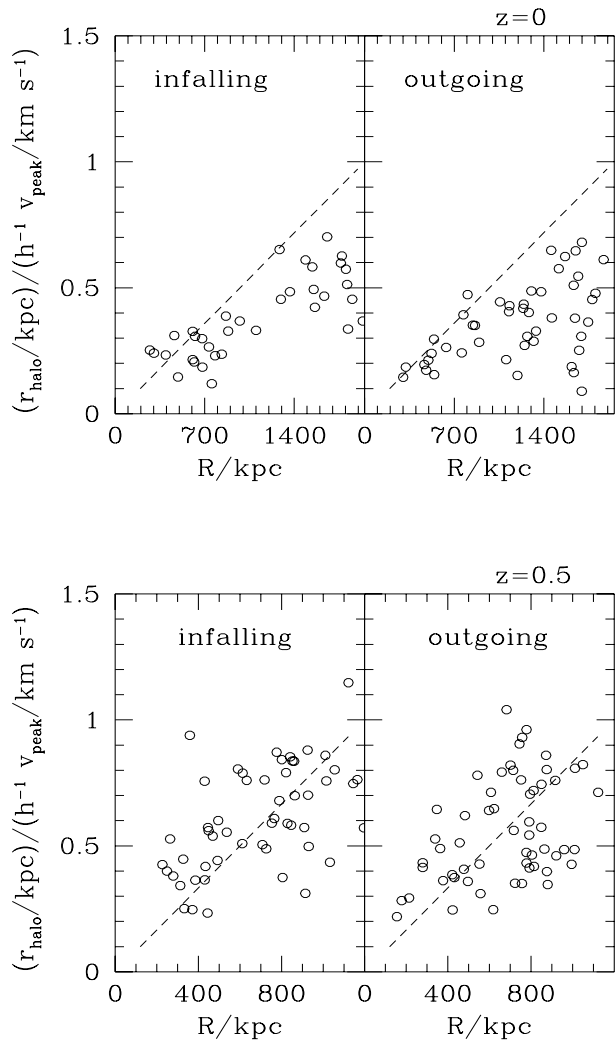


Figure 10. Same as in Figure 9 but the halo radii are measured using the SKID algorithm, that discards unbound particles, and data are shown for $z = 0.5$ too (lower panels). Only data for cluster halos are plotted; at $z = 0.5$, the formal cluster’s virial radius is $R_{200} = 1200$ kpc.

gies between ingoing and outgoing halos. Moreover, halos reaching apocenters beyond the cluster’s boundaries might be heated by low–speed encounters with other halos and re-expand, partly covering the effects of tides at the previous passage at pericenter.

The distribution of η at $z = 0$ is shown in Figure 9. It has a trend similar to that expected for locally truncated isothermal spheres (dashed line). The separation between the latter and the points in the “periphery” ($R > 2$ Mpc) is a measure of the departure of the actual density profiles of peripheral halos from isothermal. All outgoing halos must have necessarily passed their pericenters; therefore, η should depart from the dashed line more than those for infalling halos and we do observe evidence of this effect in the Figure. The corresponding results using SKID halo radii are shown in Figure 10 which also shows results for $z = 0.5$ (only for

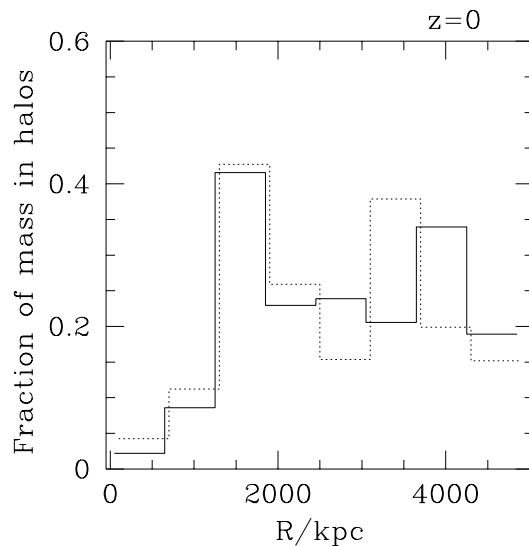


Figure 11. Fraction of mass within resolved halos in spherical shells of thickness 600 kpc versus cluster-centric position at $z = 0$. The solid line is for RUN1 and the dotted line is for RUN2 (slightly shifted for clarity).

halos with $R < R_{200}$; note the different scale on the horizontal axis from $z = 0$ to $z = 0.5$; $h = h_0(1+z)^{1.5}$ is H_z in units of $100 \text{ Mpc}/\text{km s}^{-1}$). The results for $z = 0$ confirm the general picture illustrated by the previous Figure 9, but here the points have a larger scatter and the trend with R is weaker, especially for outgoing halos: this is expected because, in the “dynamical” definition used by SKID, the tidal radii are less sensitive to $\rho_{bkg}(R)$. At $z = 0.5$, there is evidence that tidal effects are already operating at this relatively high redshift, in agreement with the trend shown by Figure 8.

4.4 Fraction of mass in halos

Figure 11 shows the fraction of the mass attached to halos. As expected, it decreases sharply approaching the cluster center: it is $\lesssim 5\%$ at $R \lesssim 500$ kpc and increases to $\sim 20\%$ at R_{200} . The total fraction of mass attached to halos within R_{200} is about 13%. (These values do not depend sensitively on the adopted value of the softening parameter.) Outside the cluster, the halos account for about 20% of the total mass. The peak at $R \sim 1.5$ Mpc is not significant: it is caused by the largest halo within the cluster of mass $2.3 \cdot 10^{13} M_\odot$ that contributes alone 5% of the total mass of the cluster and half of the mass in that bin.

We can compare the mass fraction of peripheral halos with the Press–Schechter approximation (1974), using again a routine supplied by P. Tozzi. Adopting a minimum halo mass of $1.35 \cdot 10^{10} M_\odot$ (16 particles) and the mass of the most massive peripheral halo ($3.4 \cdot 10^{12} M_\odot$), we find ~ 0.25 from the analytical theory, in good agreement with the average of the last five outer bins, ~ 0.23 .

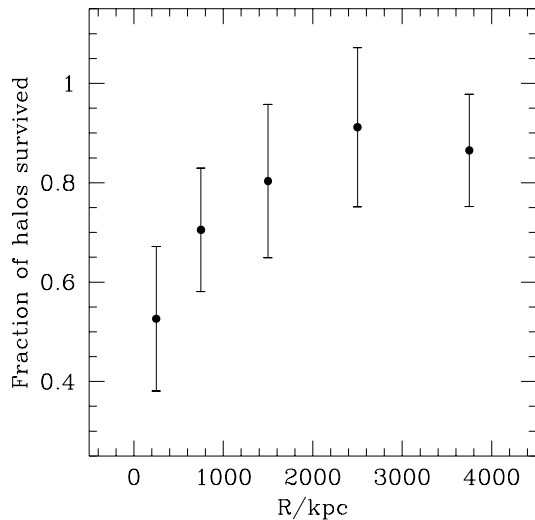


Figure 12. Fractions of $z=0.5$ halos above resolution that have survived to $z = 0$ retaining more than $\sim 50\%$ of their original masses; the errorbars are $1-\sigma$ Poissonian uncertainties estimated from the numbers of halos in each distance interval.

4.5 Merging and ‘surviving’ halos

Comparing the distribution of the halos at $z = 0.5$ and $z = 0$, we can determine the merger rate and the fraction of halos that dissolve in this interval. We selected all the halos (of RUN1) with more than 32 particles at $z = 0.5$ and examined their association with halos with more than 16 particles at $z = 0$. We determine that a high- z halo is the progenitor of a low- z halo if the latter contains at least a significant fraction of the mass of the former, say 25%. However, to account for mass loss via tidal stripping we need be less restrictive, therefore we considered also an extreme mass fraction cut-off of 1%, but our results are not very sensitive to this limit.

We find, for halos with apocenters $r_{apo} \geq R_{200}$ and at least one progenitor among those identified at $z = 0.5$, that 5–9% of them, depending on the mass fraction cut-off, are the product of a merger. There are a large number of mergers among halos with apocenters close to R_{200} (3–5 out of 17). However, of the 38 halos with $r_{apo} \lesssim 80\% R_{200}$, none has merged. We find no evidence for merging once the halos have entered the cluster. This seems to argue against the possibility of Butcher–Oemler (1978, 1984) galaxies being cluster members with star formation switched on by mergers in the cluster environment (Couch *et al* 1994).

Figure 12 shows the fraction of halos identified at $z = 0.5$ in different distance intervals that are also associated with $z = 0$ halos. Although we adopt the extreme 1% mass fraction cut-off to establish this association, the results shown in the Figure essentially give the probability that halos will survive with 50% of their original masses attached. In fact, $z = 0.5$ halos with masses just above the limit of 32 particles will be resolved at the 16-particle limit of the $z = 0$ sample, only if they have not lost more than 50% of their masses; and these small halos dominate the statistics.

At $R \lesssim 0.5$ Mpc, such probability is ~ 0.5 , against a value of order unity in the cluster periphery.

4.6 Orbital parameters

We now shift our attention to the motions of the halos within the cluster. Halos that follow radial orbits are more likely to be disrupted than halos that have circular motions, since the former penetrate further into the cluster potential well. Do we detect a bias in favour of circular orbits? We calculate orbits by approximating the cluster potential as a spherical static potential, computed using the density profile at $z = 0$ and then using the position and velocity information for the halos. For comparison, we also compute the orbits of a random subset of 20,000 particles.

In the upper panel of Figure 13 we plot the ratios r_{peri}/r_{apo} vs R for the halos of RUN2 (RUN1 gives identical results). The lower panel shows the average values of this ratio for the halos (solid line) and the particle sample (dotted line). The errorbars show $1-\sigma$ standard deviations. We find that radial orbits are quite common and circular orbits are rare. The median ratio of apocenter:pericenter is approximately 6:1 and nearly 25% of the halos are on orbits more radial than 10:1. A rough calculation by the authors reveals that this is very close to an isotropic orbital distribution within an infinite isothermal potential.

We do not detect a large difference between halo orbits as a function of R , nor do we find a difference between the orbits of the particle background and the halos. This is surprising since we expected to find fewer halos on radial orbits near the cluster center. The expected bias could be disguised if the central overmerging problem originated within the dense clumps that formed before the final cluster. Finally, we note that the radial velocity dispersion of the halos within the cluster is 720 km s^{-1} , a value that is within a few percent of the dispersion of the background particles – even when only the most massive halos are considered.

Information on the distribution of the orbital parameters of halos can be used to model the effects of tidal stripping and dynamical friction for halos within halos in semi-analytic models of structure formation based on the Press–Schechter approximation. Figure 14 and 15 plot the probability density distributions of ‘circularities’ and pericenters for cluster (solid line) and peripheral (dashed) halos. For each halo, the ‘circularity’ $\epsilon \equiv J/J_C(E)$ is defined as the ratio of its angular momentum to that of a circular orbit with the same energy (Lacey & Cole 1993). There are no marked differences between the two groups of halos, although the orbits of cluster halos are more close to circular and penetrate further into the cluster than those of peripheral halos. Among the latter, 15% have pericenters outside the cluster’s boundaries and 9% come as close as 200 kpc ($0.1R_{200}$) to the cluster’s center. This condition is twice more frequent among cluster halos; in the whole sample the fraction of $r_{peri} < 200$ kpc is 14%. These results are in good agreement with results presented by Tormen (1997).

For such radial orbits, we expect that the tidal radii of the halos are determined primarily by the global tidal field of the cluster. We can check if this is correct by estimating the truncation radius at the pericenter of each halo using $r_{tid} \simeq r_{peri} \cdot v_{peak}/V_c$ (the use of $V_c(R)$ at $R = r_{peri}$, instead of the constant value $V_c = V_{200} = 1000 \text{ km s}^{-1}$ does

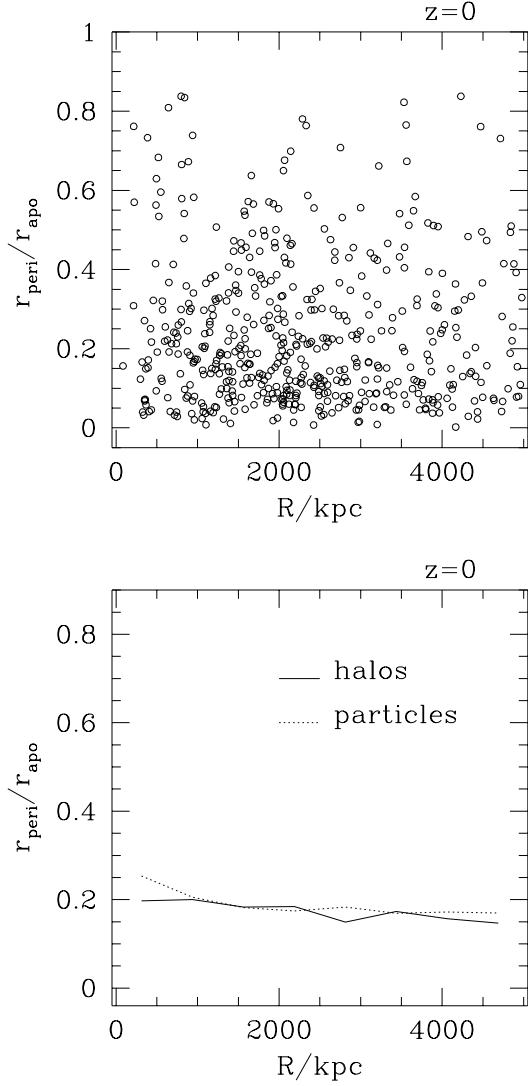


Figure 13. The upper panel shows the ratio pericentric and apocentric distances for each halo plotted against its current position. The lower panel shows the average value of these ratios for the halos (dashed curve) and a random subsample of cluster dark matter particles (solid curve). The errorbars are the dispersion about the average.

not make any detectable difference, because the variation of $V_c(R)$ is $\lesssim 10\%$ in the range $0.05 < R/R_{200} < 1$). We can test this prediction for our outgoing halos that must have passed pericenter recently, enhancing the likely validity of our approximation. In Figure 16 we plot the expected tidal radius, according to the above formula, against the value measured, for both methods (from SKID and from the circular velocity profile $v_c(r)$). The agreement is excellent for the SKID values, with the exception of the points marked as stars. These latter points represent halos that are on very eccentric orbits such that r_{peri} is less than 300 kpc: These halos are more likely to suffer impulsive collisions with other halos as they pass close to the cluster center. We note that many of these halos have tidal tails that may cause the measured tidal radii to be overestimated. The scatter in the correlation

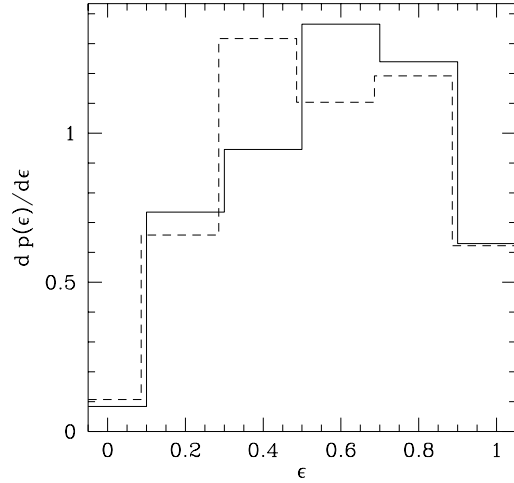


Figure 14. Probability density distribution of halo “circularities” $\epsilon \equiv J/J_C(E)$ (see text) for cluster ($R < R_{200}$; solid line) and peripheral halos (dashed).

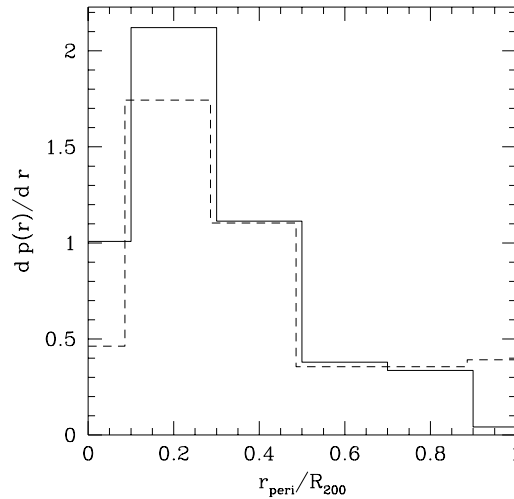


Figure 15. Probability density distribution of halo pericenters r_{peri} (line styles as in Fig. 14).

increases when we measure halo sizes using the halo circular velocity profiles, but the trend is still apparent. The radii estimated with this method are more sensitive to tidal tails than SKID radii, since the latter can discard the unbound streams of particles. This is the reason why some points in the lower panel of the Figure correspond to larger r_{tid} than those in the upper one.

Recalling Figures 9 and 10, we can now check if tidal stripping is indeed responsible for the low values of $\eta \equiv$

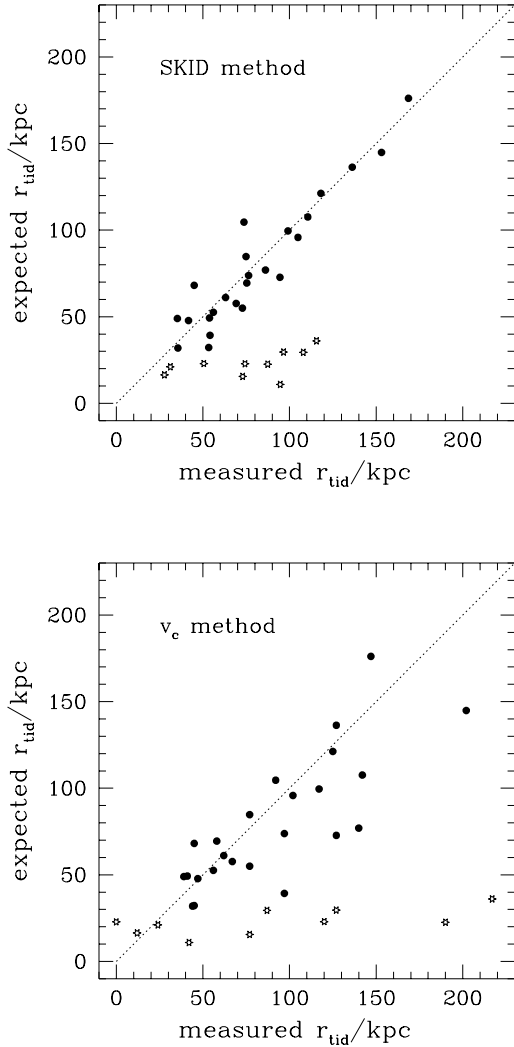


Figure 16. We plot the measured values of halo tidal radii against their expected values, assuming that the halos have isothermal mass distributions that are tidally stripped at their pericentric positions. The upper panel uses halo tidal radii measured using SKID, therefore only self-bound particles are included to determine halo sizes; the ‘ v_c ’ method uses halo circular velocity profiles and includes the cluster background. The points represent outgoing halos (at $z = 0$) with $R \leq 0.8R_{200}$; the stars denote those with $r_{peri} < 300$ kpc.

$r_{halo}/(h^{-1}v_{peak})$. Using the information on r_{peri} , we can ‘correct’ the values of η for outgoing halos as $\eta \rightarrow \eta \cdot R/r_{peri}$. The effect of this correction is shown in Figure 17, in which the open circles are the original points of the upper-right panel of Figure 10 and the filled circles are ‘corrected’. As expected, the corrected η scale as R/R_{200} . In conclusion, the isothermal model predictions for the tidal radii work well when the pericentric positions of the halos are used. In turn, this good agreement confirms that our estimates of the orbital parameters for cluster halos are correct.

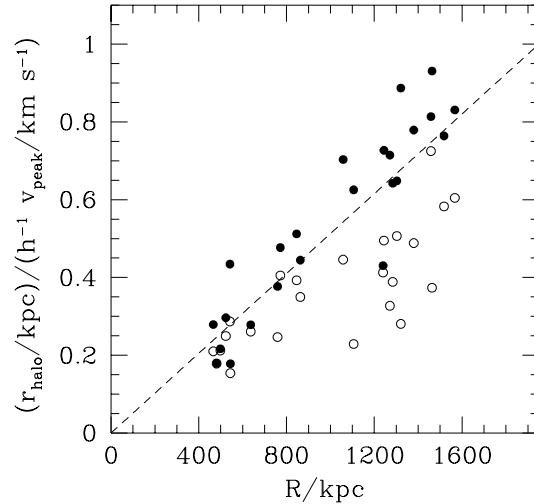


Figure 17. The dashed line gives the expected dependence on R of the ratios $\eta \equiv r_{halo}/v_{peak}$ for isothermal halos that are tidally limited by the cluster at a distance R as they fall into the cluster for the first time. Such ratios attain a minimum when halos reach pericenter and are maximally stripped; therefore, moving away from the cluster’s center, outgoing halos have values of η systematically below the line (the open circles; same as in the upper-left panel of Figure 10). If we ‘correct’ their η s using the information on their pericenters, the points are brought back to the line (the filled circles).

5 HALO INTERNAL PROPERTIES

We shall now examine the internal structure of halos in more detail with the main objective of studying how the cluster environment affects them. In particular, we shall focus on the distribution of r_{peak} and v_{peak} , that provide information on their internal concentrations. Then, we shall study in detail a small subsample of well resolved halos and examine their density profiles and the compatibility with the analytic fits generally adopted in the literature to describe dark matter halos (Hernquist 1990; Navarro, Frenk & White 1996).

5.1 Statistical distribution of halo properties

A detailed analysis of isolated cold dark matter halos in N -body simulations has been carried out by Navarro, Frenk & White (1996 and 1997, NFW in the following). Their simulations had a mass resolution such that individual halos contained of order 10,000 particles and force softening that was 1% of the final virial radii. Over a wide range of masses, NFW found relations between the properties of their profiles, r_{peak} and v_{peak} and their virial masses M_v . Furthermore, the density profiles of halos could be fit by a universal formula with varying concentrations, c , that can be predicted from their masses within a given cosmological model.

Here we want to address two questions:

(i) Do the same relations found by NFW for isolated halos hold for the *peripheral halos* that surround the virialized

cluster? These are relatively isolated, but they evolved in an environment that is special owing to the nearby cluster. For instance, the streaming motions it induces could have determined peculiar merging histories of the peripheral halos, and merging may play a crucial role in shaping their internal structures (cfr. Syer & White 1997; Moore *et al* 1997).

(ii) Do the same relations apply for *cluster halos*, that are affected by tidal stripping and halo–halo encounters? Cluster halos could also have peculiar properties reflecting the high–density environment in which they formed.

These two factors could then affect the properties of our halo sample in such a way that, for instance, the ratios v_{pk}/r_{pk} , that reflect the concentrations of the halos, are systematically higher than for the field population (e.g. cluster halos form earlier or are biased towards high concentrations such that they have survived tidal disruption) Alternatively, impulsive mass loss may cause halos to subsequently “relax” and re–expand towards an ‘equilibrium’ configuration. This could be detected as a change in concentration versus orbital position.

We shall focus on the following two relations, for cluster and peripheral halos, M_{halo} vs. v_{peak} and r_{peak} vs. v_{peak} . The former has the interest of relating masses to velocities, that are in principle more easily observable, whilst the latter gives information on halo concentrations and the related issues discussed above.

The distribution of halo masses vs. v_{peak} is illustrated in Figure 18, for peripheral (upper) and cluster halos (lower panel) and compared with the relation found by NFW within the cosmological model we have adopted (NFW 1996; dashed line). (For clarity, only points with $v_{peak} > 100 \text{ km s}^{-1}$ are shown, since the noise is large for small halos). In each panel, the stars mark *inner* halos of each group (see the caption of the Figure for details; note that some inner halos within the present “periphery” sample have highly radial orbits and were inside the cluster at an earlier epoch.) For peripheral halos, the agreement between our data and the NFW curve is excellent (note that most of the scatter owes to points with $v_{peak} < 150 \text{ km s}^{-1}$ that may be affected by the numerical noise). Cluster halos have a much larger scatter and the fit is shallower. Their masses are smaller for a given v_{peak} , as naturally expected for stripped halos and this is most noticeable for the *inner* cluster halos.

The distribution of v_{peak} and r_{peak} is shown in Figure 19, again for peripheral halos in the upper panel and cluster halos in the lower panel. The dashed line gives the relation for the halos studied by NFW and the dotted line in the upper panel is a power–law fit to the halos with $v_{peak} > 150 \text{ km s}^{-1}$ (that appear to be less affected by noise). The behaviour of the peripheral halos clearly agrees well, within the scatter, with that expected from the analysis of NFW. On the contrary, cluster halos lie significantly below the dashed line: they are skewed towards smaller values of r_{peak} for a given v_{peak} , with a more prominent effect for the innermost halos.

At $z = 0.5$, we observe a behaviour similar to that at $z = 0$, as is shown in Figures 20 and 21 (in these figures, the dotted line is again a fit to the points with $v_{peak} > 150 \text{ km s}^{-1}$ and the dashed line, the NFW’s relation at $z = 0$, is drawn for comparison).

In conclusion, the high–density regions of the cluster and the “accelerated collapse” of the cluster halos can affect

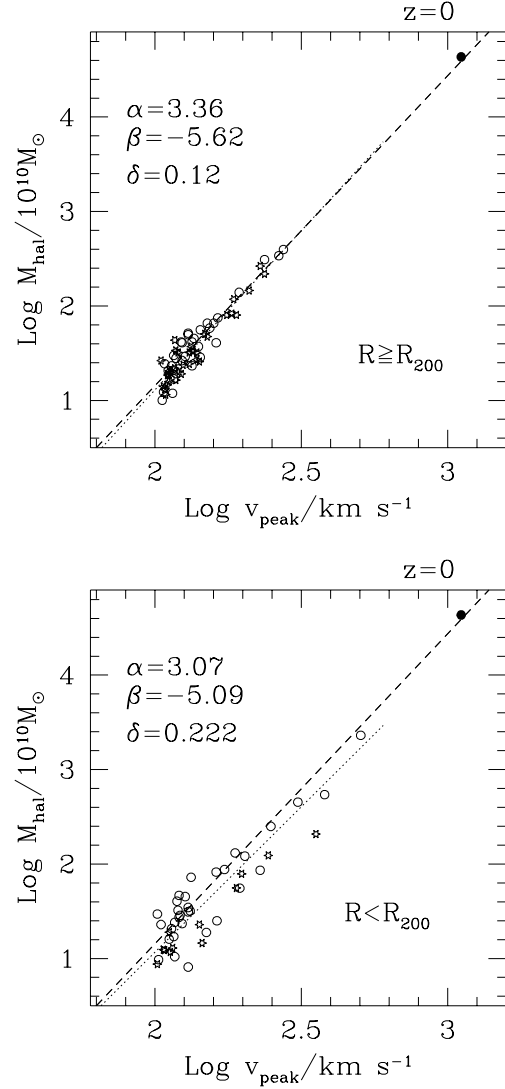


Figure 18. Distribution of halo masses versus v_{peak} for ‘peripheral’ (upper panel) and cluster halos (lower panel) at $z = 0$. The stars mark inner points, with $R < 1.5R_{200}$ and $R < 0.6R_{200}$, respectively for the two groups. The filled circle gives the values for the entire cluster. The dashed line is the power–law fit obtained by Navarro *et al* (1996) for isolated halos. The dashed lines are similar power–law fits to the data of the form $M = 10^\beta v^\alpha$, where δ is the rms scatter in mass about the fit.

not only the sizes of the halos but also their internal structures. We examine this issue further in the next section by looking in detail at the properties of a sample of large well resolved halos.

5.2 The large halo sample

We now restrict our analysis to several well resolved, massive halos that are not as affected by force softening or mass resolution, by following the evolution of those halos that have $r_{peak} > 25 \text{ kpc}$ and $v_{peak} > 150 \text{ km s}^{-1}$ (from Figure 19, we can see that these values delimit a region in the plane

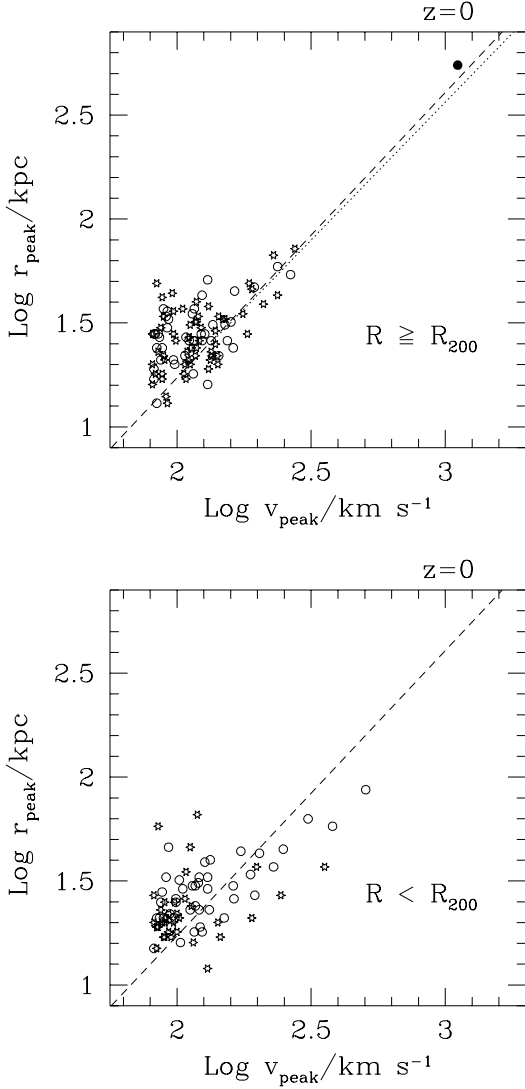


Figure 19. Distribution of v_{peak} and r_{peak} for peripheral (upper panel) and cluster halos (lower panel) at $z = 0$. The points have the same meanings as in Figure 18. As before, the dashed line gives the expected relation for isolated halos (Navarro *et al* 1996) and the dotted line is a fit to the points with $v_{peak} \geq 150 \text{ km s}^{-1}$.

(v_{peak}, r_{peak}) where the properties of halos behave quite regularly).

To highlight differences between “cluster halos” and “peripheral halos”, we selected two groups in the distance ranges $R/R_{200} \leq 2/3$ and $4/3 < R/R_{200} < 7/3$. Again, these values of R correspond to those roughly separating different halo behaviours in Figure 19. These selection criteria yield 7 halos in the first distance range (although names like “Yogi”, etc... would be preferable, for brevity’s sake, we shall simply call them: A, B, C, D, E, F) and 7 in the second one (G, H, I, L, M, N, O). The first 3 of each group lie in the inner part of their distance ranges ($R \lesssim 0.8 \text{ Mpc}$ and $2.8 \text{ Mpc} \lesssim R \lesssim 3.5 \text{ Mpc}$, respectively). All of these halos contain at least 1000 particles within r_{halo} . We excluded halo “O” because it is the product of a recent merger ($z \sim 0.5$).

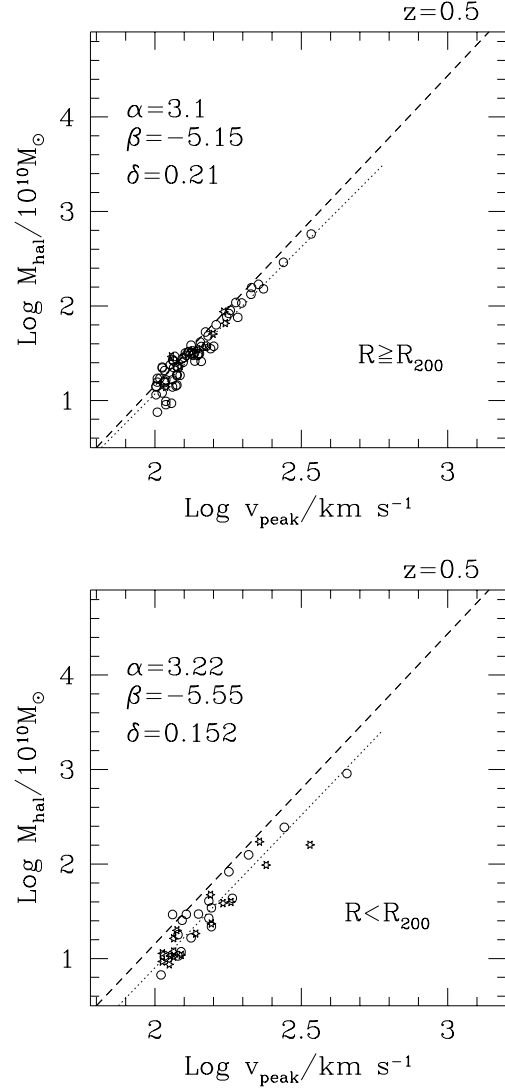


Figure 20. Symbols and lines are the same as in Figure 18 but for $z = 0.5$. Here, R_{200} is the formal cluster’s virial radius at that epoch.

All of the other halos have only one progenitor at $z = 0.5$ and the inner halos are well defined up to $z \sim 2$.

5.2.1 Evolution of the profiles

We now examine the evolution of the density profiles for this sample of halos. We consider four values of the redshift: $z = 0$, $z = 0.5$, $z = 1$, and $z = 1.8$. In our sample, all peripheral and *outer* cluster halos show evidence of major mergers at $z \sim 1$, but the inner cluster halos (A to D) have a well defined major progenitor up to $z = 1.8$ (although they have captured many small satellites and experienced minor mergers since $z \sim 1$). For peripheral and outer cluster halos we limit our analysis to $z = 0.5$, while for the innermost ones we will examine the profile data up to $z = 1.8$.

Figure 22 shows the evolution of $\rho(r)$ for the cluster halos. All the curves for the present epoch flatten at large r

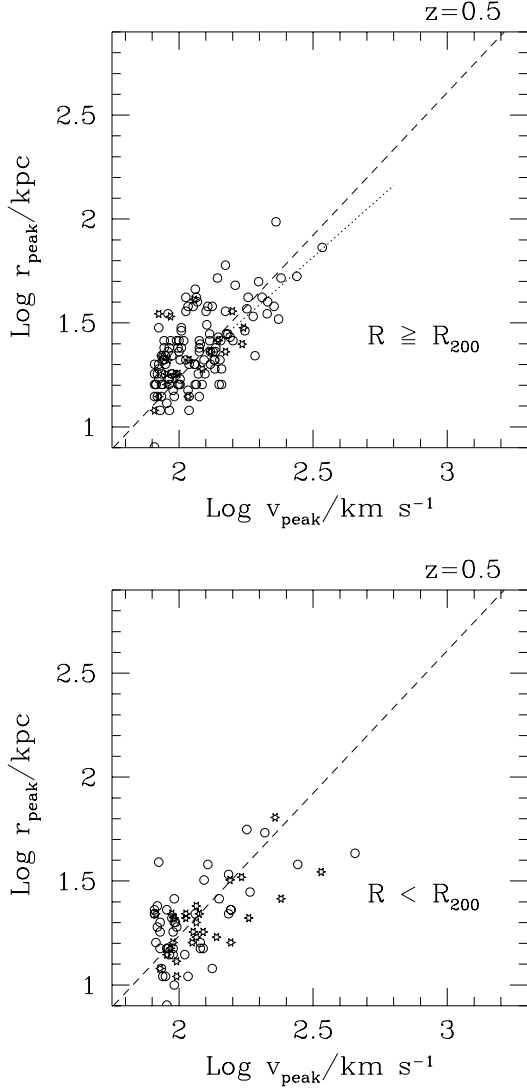


Figure 21. Symbols and lines are the same as in Figure 19 but for $z = 0.5$. Here $R_{200} = 1.2 \text{ Mpc}$ is the formal cluster’s virial radius at that epoch.

where the smooth particle background density of the cluster, ρ_{bkg} , starts dominating (halos from left to right in each row of figures have increasing distances from the cluster center). Such flattening also appears in the profiles of the $z = 0.5$ progenitors of A, B and C because they are within the high density environment of the forming cluster at that epoch.

The features of $\rho(r)$ are highlighted in the corresponding circular velocity profiles $v_c(r)$ shown in Figure 23. Note that the location and height of the peak of $v_c(r)$ have both changed for the *inner* halos (upper panels), whilst the profiles of the *outer* halos E and F, in the lower row, are remarkably stable, apart from the change in ρ_{bkg} .

Halos A and D show the most significant evolution and have quite steep outer slopes. Halo A formed at the intersection of the two filaments whose collapse originated the cluster and its structure has been heavily disrupted by the tidal field there, causing it to lose a huge amount of mass. Halo D formed in the outer parts of one of the filaments, and

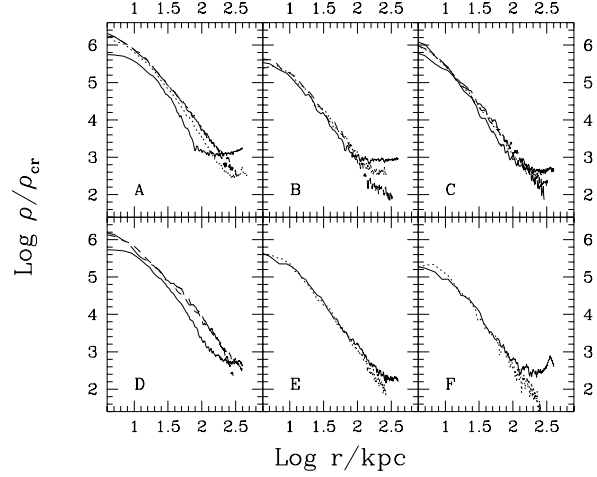


Figure 22. Evolution of the density profiles of a sample of massive cluster halos after their last major mergers. The solid, dotted, short-dashed and long-dashed lines are the profiles measured at $z = 0, 0.5, 1, 1.8$ respectively (some halos have their last major mergers at $z \geq 1$ and correspondingly, not all lines are shown; the $z = 0.5$ profile of D could not be measured because this halo was too close to the cluster’s center at that epoch). The radius r is the distance from the halo centers in physical kpc and ρ is measured in units of today’s critical density $\rho_{0,cr}$.

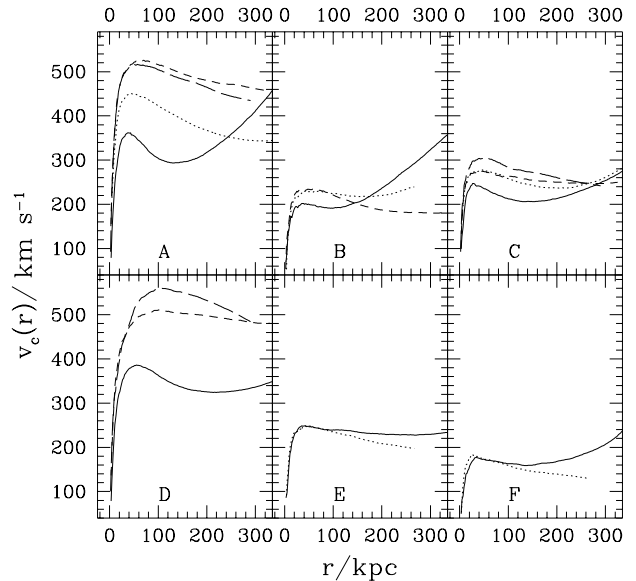


Figure 23. Evolution of the circular velocity profiles for the same halos as in Figure 22, plotted using the same line types at the different redshifts. The velocities are measured in physical km s^{-1} .

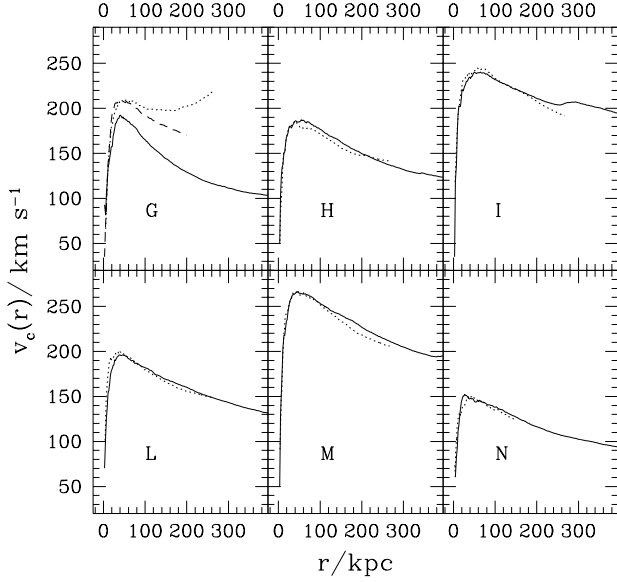


Figure 24. Evolution of the circular velocity profiles of a sample of peripheral halos after their last major mergers. The dotted and short-dashed lines correspond to the redshifts $z = 0, 0.5, 1$. (At $z = 0$, halo G has a distance from the cluster’s center $\sim 4/3R_{200}$ but was inside the cluster at earlier epochs.

its fate has been similar. Halos B and C have also evolved, but the changes have not been so dramatic. The values of v_{peak} have decreased however by $\sim 15\%$ between $z = 0.5$ and $z = 0$. The remaining halos E and F, that do not show signs of significant evolution, formed in the periphery, but at $z = 0$ they are moving outwards. However the pericenter of F is close to its present distance (~ 1.3 Mpc). That for E is ~ 600 kpc, yielding an expected tidal radius of ~ 150 kpc; this agrees very well with the SKID value, but is 25% smaller than the tidal radius measured from the density profile (directly from $\rho(r)$, or from $v_c(r)$). This is due to the anisotropic distribution of mass around E, that appears stretched along the orbit with a “trail” of particles on both sides. This tidal debris were contained within its virial radius at $z = 0.5$ and, though stripped during the passage at pericenter and presently unbound to it, are still moving closely apparently on the same orbit. The lack of evolution in the density profile of E is then due to the assumption of spherical symmetry and the contribution from unbound particles nearby.

Finally, Figure 24 shows the corresponding v_c profiles for the 6 peripheral halos considered. Except for case G, these halos have never entered the cluster and their profiles show no significant differences between $z = 0$ and 0.5. Halo G formed in the periphery but has been orbiting through the cluster since $z \sim 0.5$ and has clearly lost mass.

In summary, of the large cluster halos identified at $z = 0$, only those with $R \lesssim R_{200}/2$ have density profiles significantly different from those they had before the formation of the cluster. However, one of the large halos in the outskirts of the cluster has survived a passage (or more) at pericenter and has evolved considerably too. In particular,

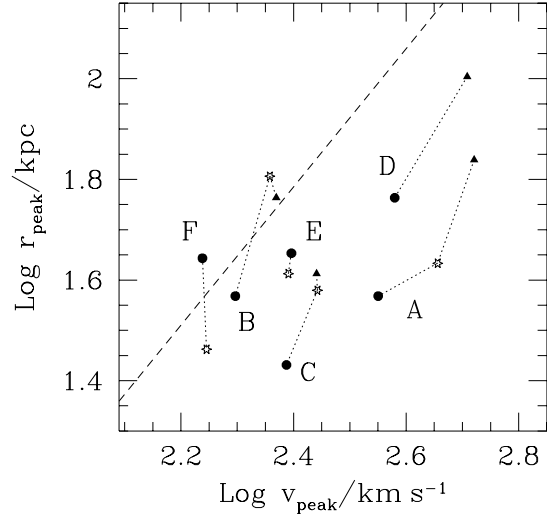


Figure 25. Evolution of the cluster halos of Figure 22 in the plane (v_{peak}, r_{peak}) . The positions at $z = 0$ are plotted as filled circles, those at $z = 0.5$ as stars (not for D) and at $z = 1$ as triangles (only for A–D). The dashed line is the relation expected for isolated halos at $z = 0$ from Navarro *et al* (1996) as in Figure 19.

the values of v_{peak} can change: $\sim 10\%$ in three cases, but 20–25% in two other cases.

It is interesting to examine how the halos “move” in the plane (r_{peak}, v_{peak}) of Figure 19, so as to determine if their evolution (under tidal stripping or halo–halo encounters) is the reason for the systematically lower r_{pk} for the cluster halos with respect to field halos of same v_{pk} . Figure 25 shows the evolution of r_{pk} vs v_{pk} for the 6 cluster halos considered previously from $z = 1$ (when available) through 0.5 to $z = 0$ (from triangles to stars in the figure). From these data, it seems that the points did not move significantly away from the NFW’s curve. They move *parallel* to the line rather than downwards and those furthest from the line are also those that formed the nearest to primordial high-density regions (A and C, that formed near the cluster’s center, but also D, that formed in one of the giant filaments that merged into it). This could be evidence that halos form earlier in high-density regions and are thus more concentrated than those forming in the field. This impression is strengthened by Figure 26, that shows the evolution of the “concentration” v_{peak}/r_{peak} (the symbols are as in Figure 25). The points on the left are for the halos forming near the center (A and C), those on the right for those forming in the periphery (B, E, F); the intermediate case D is duely in the middle. Although the ratios change, the two groups are clearly separated at both epochs with higher values of concentration for the former and lower values for the latter group. Recently, Lemson & Kauffmann (1997) have studied correlations between halo properties and local environment using large N -body simulations. Except for the mass distribution of halos, they do not find any such correlation. It should be noted however that their definition of *locality* is based on a scale of $5\text{--}10h^{-1}$ Mpc, that is still

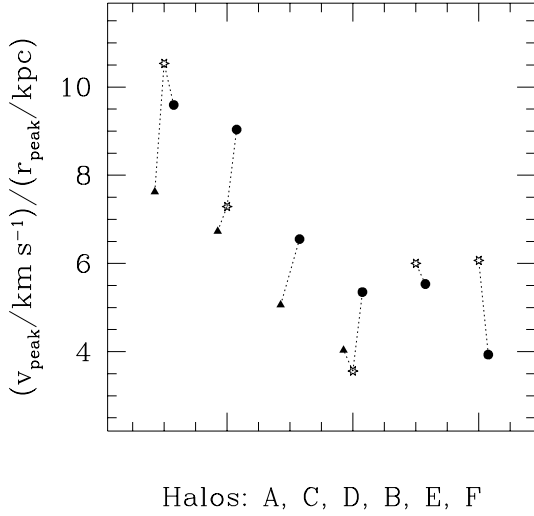


Figure 26. Evolution of “concentrations” v_{peak}/r_{peak} for the halos of Figure 25 and the points represent the same redshifts as before. The halos are ordered from left to right according to the overdensity of the region where they formed: A and B formed at the intersection of the filaments whose collapse originated the cluster, D along one of the filaments and the others in the “field”.

mildly non-linear today. The correlation we find seems to involve scales of a few Mpc that become non-linear at early epochs. It will be interesting to examine the significance of our result with larger samples of cluster halos within simulations of even higher resolution.

5.2.2 Analytic fits

The evolved density profiles of isolated halos in N -body simulations are well described for a large range of masses by the analytic model of NFW (although increasing the numerical resolution causes steeper inner profiles, Moore *et al* (1997); this is not an issue here since our sample of halos have similar resolution as those in the NFW simulations):

$$\frac{\rho(r)}{\rho_{cr}} = \frac{\delta_c}{(cr/r_{200})(1 + cr/r_{200})^2}, \quad (5.1)$$

$$\text{with } \delta_c = \frac{200}{3} \frac{c^3}{(\ln(1+c) - c/(1+c))}. \quad (5.2)$$

Navarro, Frenk & White (1997) developed an analytic procedure that gives c as a function of the halo mass M_{200} in any hierarchical cosmological model, based on the expected redshift of collapse of a density perturbation of mass M in the Press-Schechter (Press & Schechter 1974) formalism. Here we address the following two questions: (i) does the NFW profile and predicted c provide a good description of the profiles of our *peripheral halos*? As mentioned previously, this question is not trivial since the environment within which these halos evolved is perturbed by the intense gravitational field of the cluster; (ii) How much do the tidally stripped *cluster halos* depart from the NFW predictions? For example, a steeper outer slope may be typical of these halos. For

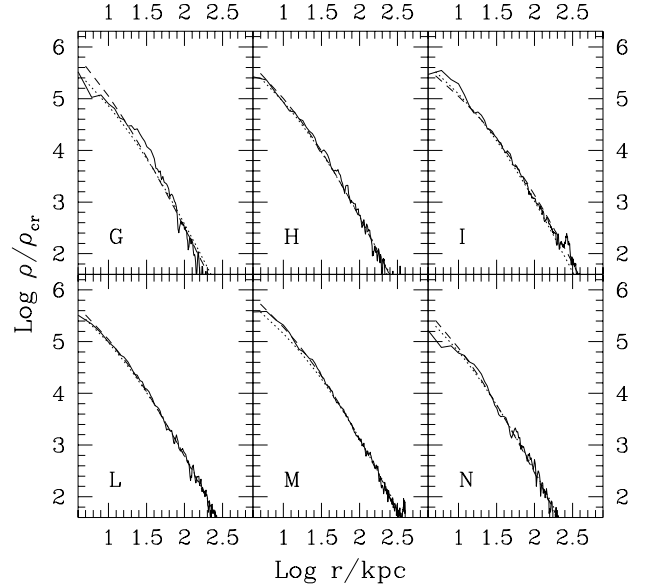


Figure 27. Comparison between the density profiles (at $z = 0$) of a sample of peripheral halos (solid lines) and the NFW model: the dotted lines are the expected NFW profiles (from halo virial masses) and the dashed lines are fits of the NFW profile to the data.

this reason, we also consider the Hernquist profile (Hernquist 1990; HER in the following):

$$\frac{\rho(r)}{\rho_{cr}} = \frac{\delta_c}{(cr/r_{200})(1 + cr/r_{200})^3}, \quad (5.3)$$

$$\text{with } \delta_c = \frac{400}{3} c(1+c)^2. \quad (5.4)$$

This profile has the same inner form as NFW, but asymptotes to r^{-4} on large scales instead of r^{-3} .

First we consider the sample of large *peripheral halos* described above. Figure 27 shows their density profiles $\rho(r)/\rho_{cr,0}$. In each panel, the *dotted* and *dashed* lines are NFW profiles *predicted* using the measured M_{200} according to the NFW procedure mentioned above, and *fit* to the data using a standard χ^2 minimization technique with c as free parameter (using r_{200} measured from the data); for the fits, we used the points in the radial range delimited by l_{soft} and r_{200} . (Two-parameter fits, with both c and r_{200} as free parameters, yield very similar results; we use two-parameter fits for the cluster halos below, since r_{200} cannot be defined for them.) We plot the residuals between the data and the NFW profiles and Hernquist profiles in Figure 28. Each panel shows the fractional difference $(\rho_{model}(r) - \rho(r))/\rho(r)$ as a function of r , where $\rho(r)$ are the data and $\rho_{model}(r)$ is the density corresponding to one of the analytic profiles considered. With the exception of halo G, the residuals for the NFW profiles are within ~ 20 – 30% at distances from the halo centers $r \gtrsim 15$ kpc. At smaller distances, the profiles of our halos are steeper than the NFW curves with residuals typically in excess of 30% for the fits and 40% for the predicted curves. Note that, for the same halo, the different NFW curves have concentrations that can differ by various amounts, typically from $c \sim 13$ – 14 (expected) to 16 – 18

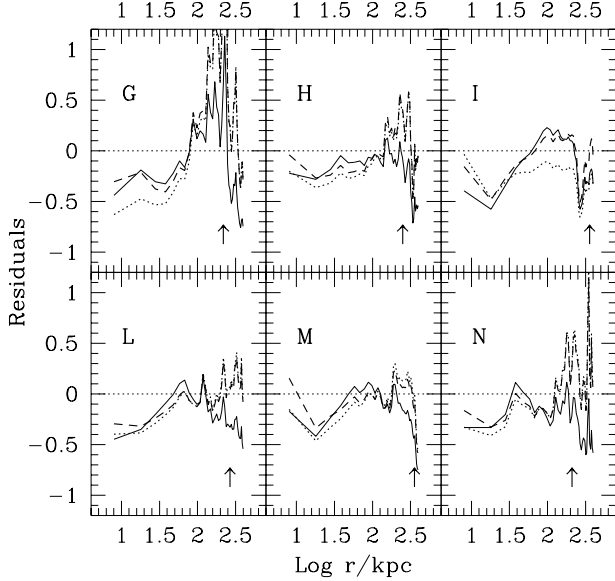


Figure 28. Residuals $(\rho_{NFW}(r) - \rho(r))/\rho(r)$ between the NFW profiles and density profiles of Figure 27 (dotted and dashed lines are again for the expected and fitted NFW profiles). The residuals of fits of the Hernquist profile to the data are shown as thin solid lines. The arrows mark the halo virial radii. (For clarity, we show 1 data point every 5).

(fits). The data do not discriminate significantly between NFW and Hernquist's profiles. Only for halo G, as expected from its steep profile, the HER fit fares better, although it still has positive residuals of $\sim 40\text{--}50\%$.

Let us now examine the *cluster halos*. Their density profiles (again solid lines) are shown in Figure 29, together with NFW (dotted) and HER (dashed) fits (for the latter, we use the data in the radial range delimited by l_{soft} and the value where $\rho(r)$ flattens approaching ρ_{bkg}). Over the scales of interest, the two fits do not differ significantly and both underestimate the central concentrations of the halos. As before, this can be seen better by examining the residuals in Figure 30. At intermediate distances from the halo centers ($r \lesssim 40$ kpc), both fits have negative residuals in excess of $\sim 20\%$, and in excess of $\sim 30\%$ on smaller scales. At larger distances, up to about 75% of the halo tidal radii, they fare generally well, with residuals well below 20%. The exception is halo A, that has, as halo G, a particularly steep profile: for this halo, HER is still an acceptable fit, while NFW has large residuals, $\sim 40\text{--}50\%$. When r approaches r_{tid} , the fits depart rapidly from the flattening $\rho(r)$, with average residuals at r_{tid} of order of 30% or more, for NFW, and about 10% higher for HER.

As a general remark to conclude this section, if we limit the halo sample to lie within $r < 3/4 r_{tid}$, Hernquist's fits are better than NFW for the profiles of cluster halos (or stripped halos in general), while the latter model fares well for peripheral halos. Although our resolution is not good enough to address reliably the issue of halo concentrations, it is remarkable that our halos are systematically more concentrated than the NFW model predicts, when from the poorer resolution we would expect just the opposite. In our anal-

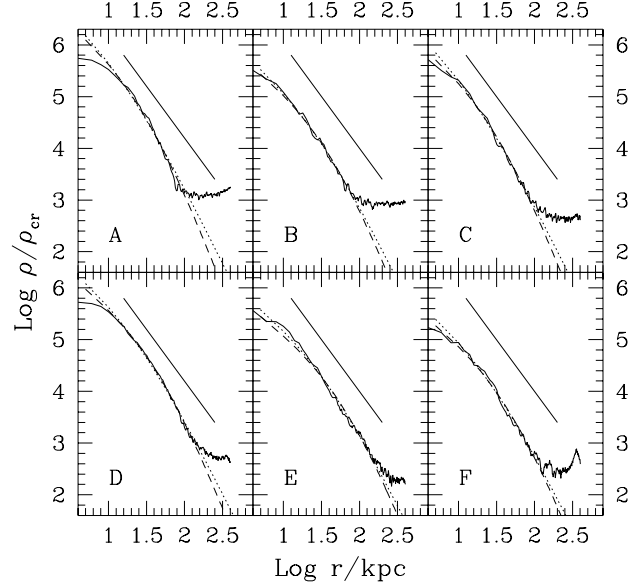


Figure 29. Comparison between the density profiles (at $z = 0$) of a sample of cluster halos (solid lines) and fits of NFW (dotted lines) and Hernquist's (dashed lines) profiles. An arbitrary isothermal profile is drawn for comparison (thin solid line).

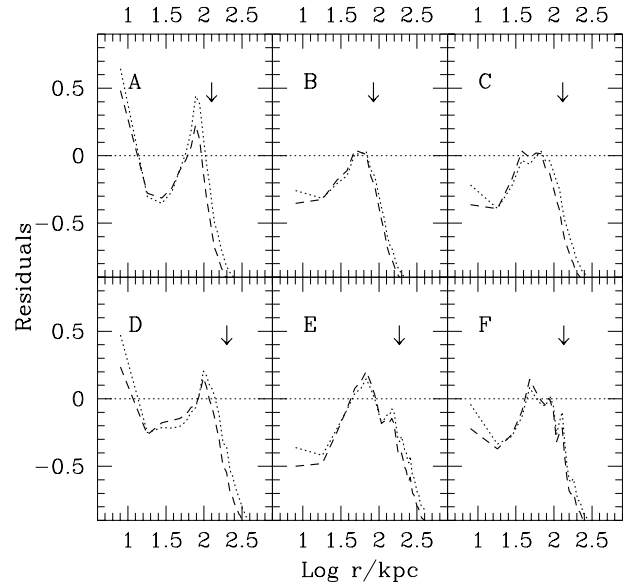


Figure 30. Residuals $(\rho_{FIT}(r) - \rho(r))/\rho(r)$ for the fits of Figure 29 (NFW, dotted line, and Hernquist, dashed). The arrows mark the halo tidal radii.

ysis, the NFW profiles fit to the data have concentrations about 25% higher than expected and still, they generally underestimate the profiles measured at small scales.

6 SUMMARY AND DISCUSSION

We have explored the consequences of increasing the force and mass resolution within a *dark matter only* simulation of a rich galaxy cluster that forms hierarchically within a cold dark matter simulation of a closed Universe. By resimulating regions of interest using increased resolution, we have attained an unprecedented view of the internal structure of a massive dark halo. With approximately one million particles within the virial radius and force softening that is 0.25% of R_{200} , we resolve 150 halos with circular velocity larger than 80 km s^{-1} within R_{200} at $z = 0$. Most of these halos have made several orbits within the cluster and are easily identified as potential minima or density enhancements above the background.

This work demonstrates that the overmerging of dark matter substructure within virialised structures can be greatly reduced given high enough numerical resolution. The statement that “at bottom the problem [of overmerging] appears to be not numerical but physical: gravitational dynamics alone cannot explain the existence of galaxy groups and clusters” (Weinberg, Katz and Hernquist 1997) is, at the light of these new results, completely wrong.

Overmerging within the cluster environment is due to the disruption of halos by the global tidal field and halo-halo encounters (*c.f.* Moore *et al* 1996), probably primarily within the large dense halos prior to the formation of the main cluster. Although our softening length (5 kpc) is a small fraction of the cluster’s virial radius, the rotation curves of the halos peak at radii of ~ 30 kpc. Hence the cores of these halos can be softened to a degree that affects their evolution. This is the primary reason the halos are still being disrupted; given high enough force and mass resolution, it should be possible to overcome *most* of the overmerging problem within CDM simulations.

The aim of this paper has been to analyse the properties and dynamics of the dark matter substructure and we find the following key results:

- The orbital distribution of substructure halos is close to that of an isotropic population of tracers in an isothermal potential; the median value of apocentric to pericentric distances is 6:1, a value that does not vary with position within the cluster and is unbiased with respect to the orbits of the smooth particle background. Circular orbits are rare and about 20% of all our surviving halos within the cluster will pass within $200 \text{ kpc} \equiv 0.1R_{200}$.
- Most dark halos are tidally truncated to a value determined by the (average) density of the cluster at their pericentric positions. The approximation of isothermal halo mass distributions orbiting within a deeper isothermal potential works very well; *i.e.* $r_{\text{tidal}} \sim r_{\text{peri}} \sigma_{\text{halos}} / \sigma_{\text{clus}}$.
- The mass attached to dark matter halos is approximately 13% of the entire cluster mass and varies from 0% within $\sim 200 \text{ kpc}$ from the cluster center, to 20% at its virial radius. This latter value is roughly the expected value for the mass attached to halos above a circular velocity of 80 km s^{-1} . Correspondingly, the sizes of halos vary with cluster centric radius, an effect that may be observable using gravitational lensing of background galaxies.
- Overmerging within the central regions of dense halos leads to a final distribution of substructure that is antibiased

(less centrally concentrated) with respect to the global mass distribution.

- The density profiles of a sample of well resolved halos indicate that those forming in the high-density regions of the collapsing cluster have higher concentrations than those found in isolated environments. We show that this is most probably due to their earlier collapse redshifts rather than the internal response of the halos to mass loss and heating from tidal stripping.
- Most of the halos within the cluster and in the cluster proximity have density profiles that are well fit by NFW profiles (Navarro, Frenk & White 1996). Halos that lose a great deal of mass through tidal stripping have outer density profiles as steep as $\rho(r) \propto r^{-4}$ (at $\approx 30\%$ of their virial radius), thus Hernquist profiles (Hernquist 1990) provide slightly better fits.
- Mergers between halos in the cluster proximity occur with a frequency of about 5–10% since $z=0.5$. In the cluster environment mergers are rare; not a single merger occurs for halos whose orbits are contained within $1.6 \text{ Mpc} \equiv 80\% R_{200}$ from the cluster center.

ACKNOWLEDGMENTS

We would like to thank R. Carlberg, A. Jenkins, J. Navarro, G. Tormen and S. White for interesting discussions. SG was supported by the University of Milano. BM is supported by the Royal Society. FG acknowledges a fellowship from the EU network for Galaxy Formation and Evolution. We are grateful to Paolo Tozzi and Julio F. Navarro for kindly supplying fortran routines. The numerical simulations were carried out at the Denali Arctic Supercomputing Centre, the IBM SP-2 at the Cornell Theory Center, and on the Cray T3E at the Pittsburgh Supercomputing Center with support from an NSF Metacenter grant.

REFERENCES

- Bahcall, N. A., Fan, X. & Cen, R. (1997), ApJ, 485L, 53
 Bartelmann, M., Huss, A., Colberg, J. M., Jenkins, A. & Pearce, F. 1997, A & A, submitted (astro-ph/9707167)
 Baugh, C. M., Cole, S., Frenk, C. S. (1996), MNRAS, 283, 1361
 Borgani, S., Da Costa, L. N., Freudling, W., Giovanelli, R., Haynes, M. P., Salzer, G. & Wegner, L. 1997a, ApJL, 482, 121
 Borgani, S., Gardini, A., Girardi, M. & Gottlöber, S. 1997b, New. A., 2, 119
 Bower, R. G. (1991), MNRAS, 248, 332
 Brainerd, T. G., Goldberg, D. M. & Villumsen, J. V. 1997, ApJ, submitted (astro-ph/9706165)
 Carlberg, R.G., 1994, ApJ 433, 468
 Carlberg, R.G. & Dubinski J. 1991 ApJ, 369, 13
 Carlberg, R. G., Yee, H. K. C., Ellingson, E., Abraham, R., Gravel, P., Morris, S. & Pritchet, C. J. 1996, ApJ, 462, 32
 Carlberg, R. G., Yee, H. K. C., Ellingson, E. 1997, ApJ, 478, 462
 Carlberg, R. G. *et al* 1997, ApJL, in press (astro-ph/9703107)
 Cavaliere, A. & Menci, N. 1994, ApJ, 435, 528
 Cen, R. 1997, ApJ, 485, 39
 Couch, W. J., Ellis, R. S., Sharples, R. M. & Smail I. 1994, ApJ 430, 121
 Crone, M. M., Governato F., Stadel, J., Quinn, T. 1997, ApJ, 477L, 5

- Davis, M., Efstathiou, G., Frenk, C.S. & White, S.D.M. 1985, ApJ 292, 371.
- Eke, V. R., Cole, S. & Frenk, C. S. 1996, MNRAS, 282, 263
- Eke, V.R., Navarro, J.F., & Frenk, C.S. 1997, astro-ph 9708070
- Evrard, A. E., Summers, F.J. & Davis, M. 1994, ApJ, 422, 11
- Evrard, A. E. (1997), MNRAS, submitted (astro-ph 9701148)
- Frenk, C. S., Evrard, A. E., White, S. D. M. & Summers, F. J. 1996, ApJ, 472, 460
- Geiger, B. & Bartelmann, M. 1997, MNRAS, submitted (astro-ph/9707044)
- Gelb, J. M. & Bertschinger, E. 1994, ApJ, 436, 467
- Hernquist, L. 1990, ApJ, 356, 359
- Klypin, A., Gottlöber, S. & Kravtsov, A. 1997, ApJ, submitted (astro-ph/9708191)
- Lacey, C. & Cole, S. 1993, MNRAS, 262, 627
- Lemson, G. & Kauffmann, G. 1997, MNRAS, submitted (astro-ph/9710125)
- Moore, B., Katz, N. & Lake, G. 1996, 456, 455
- Moore, B., Governato, F., Quinn, T., Stadel, J. & Lake, G. (1997), ApJL, submitted (astro-ph 9709051)
- Natarajan, P., Kneibb, J. P., Smail, I., Ellis, R. S. 1997, ApJL, submitted (astro-ph 9706129).
- Navarro, J. F., Frenk, C. S. & White, S. D. M. 1996, ApJ, 462, 563
- Navarro, J. F., Frenk, C. S. & White, S. D. M. 1997, ApJ, in press (astro-ph/9611107)
- Press, W. H. & Schechter, P. 1974, ApJ, 187, 425
- Quinn, T., Katz, L., Stadel, J. & Lake, G. (1997), preprint (astro-ph 9710043)
- Rosati, P., Ceca, C.R., Norman, C. & Giacconi, R., 1998. ApJLetters 492, L21.
- Smail, I., Ellis, R. S., Dressler, A., Couch, W. J., Oemler, A. Jr., Sharpless, R. M., Butcher, H. 1997, ApJ, 479, 70
- Stadel *et al* 1998 in preparation
- Summers, F. J., Davis, M. & Evrard, A. E. 1995, ApJ, 454, 1
- Syer, D. & White, S. D. M. 1997, MNRAS, submitted, (astro-ph/9611065)
- Tormen, G. 1997, MNRAS, 290, 411
- Tormen, G., Diaferio, A. & Syer, D. 1998, MNRAS, submitted (astro-ph/9712222)
- Weinberg, D.H, Katz, N., Hernquist L. 1997, to appear in Origins, eds J.M. Shull, C.E. Woodward & H. Thronson, ASP Conference Series. (astro-ph 9708213)
- White, S. D. M., Navarro, J. F., Evrard, A. E. & Frenk, C. S. (1993), Nature, 366, 429
- Wilson, G., Cole, S. & Frenk, C.S. 1996, MNRAS, 282, 501
- White, S.D.M., Davis, M., Efstathiou, G. & Frenk, C.S. 1987, Nature 330, 451
- Wu, X.-P. & Fang, L.-Z. H. I. 1997, ApJ 483, 62

This figure "figure1.jpg" is available in "jpg" format from:

<http://arxiv.org/ps/astro-ph/9801192v1>